Actomyosin controls planarity and folding of epithelia in response to compression

Tom P. J. Wyatt[†1,2], Jonathan Fouchard[†1], Ana Lisica[1], Nargess Khalilgharibi[1,2], Buzz Baum[*3,4], Pierre Recho[5,6], Alexandre J. Kabla[*6], Guillaume T. Charras[*1,4,7]

†co-first authors: these authors contributed equally.

(1) London Centre for Nanotechnology, University College London, Gower Street, London WC1E 6BT, UK
(2) Centre for Computation, Mathematics and Physics in the Life Sciences and Experimental Biology (CoMPLEX), University College London, Gower Street, London WC1E 6BT, UK
(3) MRC Laboratory for Molecular Cell Biology, University College London, Gower Street, London WC1E 6BT, UK
(4) Institute for the Physics of Living Systems, University College London, Gower Street, London WC1E 6BT, UK
(5) LIPhy, CNRS–UMR 5588, Université Grenoble Alpes, F-38000 Grenoble, France
(6) Department of Engineering, Cambridge University, Cambridge CB2 1PZ, UK
(7) Department of Cell and Developmental Biology, University College London, Gower Street, London WC1E 6BT, UK

*Corresponding authors: Buzz Baum (b.baum@ucl.ac.uk), Alexandre Kabla (ajk61@cam.ac.uk) and Guillaume Charras (g.charras@ucl.ac.uk)

Abstract

Throughout embryonic development and adult life, epithelia are subjected to compressive deformations. While these have been shown to trigger mechanosensitive responses such as cell extrusion and differentiation, which span tens of minutes, little is known about how epithelia adapt to compression over shorter timescales. Here, using suspended epithelia, we uncover the immediate response of epithelial tissues to the application of in-plane compressive strains (5-80%). We show that fast compression induces tissue buckling followed by actomyosin-dependent tissue flattening which erases the buckle within tens of seconds, in both mono- and multi-layered epithelia. Strikingly, we identify a well-defined limit to this response, so that stable folds form in the tissue when compressive strains exceed a 'buckling threshold' of ~35%. A combination of experiment and modelling shows that this behaviour is orchestrated by adaptation of the actomyosin cytoskeleton as it re-establishes tissue tension following compression. Thus, tissue pre-tension allows epithelia to both buffer against deformation and sets their ability to form and retain folds during morphogenesis.

Epithelial tissues are frequently subjected to in-plane compression during adult life and embryonic development, as the result of both intrinsic and extrinsic forces[1–4]. These forces are central to the function of many organs and are crucial for sculpting complex tissue shapes during developmental morphogenesis[5–7]. For example, in the airway, epithelia are subjected to periodic area changes during normal breathing and to longer term compression during diseased states such as asthmatic bronchial contraction[8,9]. During embryonic development, compression guides a number of morphogenetic events involving tissue bending and folding, such as the formation of the optic cup[6], gut villi[7], and cortical convolutions in the brain[10].

Recent work has suggested that epithelia have evolved a variety of cellular-scale mechanisms to detect and respond to compression via mechanotransduction[11]. For example, compressive deformations can activate signalling pathways that regulate cell differentiation[3,12]. Moreover, cultured and primary epithelial monolayers can respond to increases in their density induced by compression by triggering the extrusion of live cells[13,14].

In vivo, epithelia are subjected to deformations lasting milliseconds to hours[15]. Yet, cellular-scale adaptive processes typically necessitate hours. Whether and how epithelia respond to compression at shorter time-scales is poorly understood. Although remodelling of the cell structure through biomolecular signalling cascades may be too slow to respond at the shortest of time-scales, recent work has revealed rapid adaptive responses emerging directly from the mechanical properties and dynamic organisation of actomyosin[16–18].

Here, to investigate the response of epithelia to compressive strain, we use suspended epithelia devoid of a substrate. This enables study of the intrinsic response of the cells without mechanical interference from the extracellular matrix (ECM). We find that both mono- and multi-layered epithelia can accommodate compression up to a well-defined limit of ~-35% strain, the buckling threshold. Up to this threshold, actomyosin-generated pre-tension allows the tissues to actively retain a planar morphology during slow compressive strains and erases buckles induced by faster strains within tens of seconds. Tissue tension decreases linearly with compressive strain, approaching zero at the buckling threshold, at which point stable folds are formed in the tissue. The observed tissue behaviours can be recapitulated by modelling epithelia as pre-tensed visco-elastic sheets which exhibit a buckling instability upon entering compression. Finally, we show that the buckling threshold is determined by the ratio between tissue pre-tension and tissue elasticity, as predicted by our model.

Results

Fast mechanical adaptation of epithelia to compression

To investigate the cell-intrinsic response of epithelia to compressive strains, we used cultured MDCK epithelial monolayers devoid of a substrate[19–21] (Fig. 1a). It is well understood from classical mechanics that slender elastic materials subjected to compressive strains will buckle, that is, they will undergo bending after a critical point. Here, after a step of -35% strain ('device strain', Fig. 1a) applied at high strain rate (500%.s^{-1}), most suspended MDCK monolayers took on an arched shape (Fig. 1b (i) and Supplementary Fig. 1a (i)), reminiscent of buckling in solid materials. Less frequently, epithelia adopted a transient wave-like shape, similar to the second mode of buckling,

before rapidly transitioning to the arched shape (Supplementary Fig. 1a-c and Supplementary Information-Appendix 1).

Remarkably, the buckles were not stable configurations. Instead the epithelia rapidly erased buckles, becoming planar within ~1 minute (Fig. 1b (i) and Supplementary Video 1). To quantify the evolution of tissue strain, we extracted the contour length of the tissue cross-section and compared it to its value before strain application (Supplementary Fig. 1d). Following application of a step of compressive strain, tissue strain first decreased rapidly before gradually slowing as the tissue approached a planar configuration (Fig. 1c). The average half-life of the flattening process was $T_{1/2}$ = 4.8 ± 0.8 s (n = 17).

To determine the limit of this adaptive process, we applied a larger strain (-50%) at the same strain rate. The tissues exhibited the same initial flattening behaviour but could not completely accommodate the larger deformation (Fig. 1b (ii), Fig. 1d and Supplementary Video 2). As a result, a buckle remained which was stable for over 10 minutes (Supplementary Fig. 1e). Overall, the reduction of contour length after compression applied at high strain rate saturated at -34 ± 8 % (Fig. 1e).

The presence of such a limit suggests that the tissue may possess a reference length, independent of time. To test this, the tissue strain was measured during a large compression applied at a low strain rate (80% at 0.5 $\%.s^{-1}$). Here, the epithelium maintained a planar morphology for large deformations until taking on an arched shape, at which point its length did not decrease any further (Fig. 1b (iii), Fig. 1f and Supplementary Video 3). The maximum tissue strain here was -33 ± 8 %, indistinguishable from the maximum deformation after fast application of compression (p = 0.45, Fig. 1e). Similar results were obtained when we sequentially applied a fast and slow deformation to the

same monolayer with 6 minute intervals (Supplementary Fig. 1f). This enabled us to define a tissue-intrinsic maximum strain, the buckling threshold ε_b, above which the tissue cannot decrease its contour length.

Interestingly, suspended multi-layered epithelia (HaCaT human keratinocytes) showed the same phenomenology (Fig. 1b (iv)-(vi), Supplementary Fig. 2a-d, Supplementary Videos 4-6) with a buckling threshold and average half-life of flattening indistinguishable from MDCK monolayers (Fig. 1e, ε_b = -38 ± 7 %, $T_{1/2}$ = 2.7 ± 0.7 s, p = 0.23 and 0.07, respectively). Again, the buckling threshold did not depend on the loading regimen (Fig. 1e and Supplementary Fig. 1f). Therefore, the rapid response to compression is not specific to a particular cell type or tissue architecture and may be a generic property of epithelia. In addition, neither the half-life of flattening nor the buckling threshold correlated with cell density (Supplementary Fig. 2e,f). Thus, epithelial tissues rapidly adapt to large in-plane compressive strains by reducing their length up to a well-defined limit, the buckling threshold, which is independent of the history of deformation.

Tissue flattening depends on actomyosin contractility

To verify that cell-scale phenomena such as oriented divisions and extrusions are not involved in flattening, we acquired images of the cell-junction network before and after compression. The junctional network before compression could be recapitulated by applying a stretch equal to the applied strain to the image of the network after compression (Supplementary Fig. 3a). Thus, changes in cell shape alone account for the changes in tissue shape. In both MDCK and HaCaT tissues, compression led to a decrease in cell length along the axis of compressive strain (x) which closely matched the tissue deformation, while the cell length along the perpendicular (y) axis remained unchanged

and cell height (z) increased (Fig. 2a,b and Supplementary Fig. 3b). In sum, the changes in cell shape fitted a model of constant cellular volume (Fig. 2b, dashed lines).

Since actomyosin activity drives both shape changes[22] and stress relaxation in single cells[23], we explored the role of actomyosin in tissue flattening. For this, we repeated the compression experiments in the presence of inhibitors of actomyosin. While all tissues still buckled upon fast compression, flattening was severely compromised (Fig. 2c (i), 2d and Supplementary Fig. 3d,e, Supplementary Video 7). Firstly, consistent with the role of actomyosin in driving stress relaxation, the rate of flattening was reduced by inhibition of contractility (Fig. 2d and Supplementary Fig. 3d-g). Secondly and more surprisingly, the tissue's ability to accommodate strain saturated at smaller values (Fig. 2d,e), showing that the buckling threshold itself depends on actomyosin. Conversely, increasing contractility with calyculin A, a phosphatase inhibitor known to increase myosin II activity, increased tissue flattening rate and buckling threshold (Fig. 2d,e and Supplementary Fig. 3g). In addition, HaCaT human keratinocytes showed the same response to inhibition of contractility as MDCK (Fig. 2c (ii), 2e and Supplementary Fig. 3g,h).

These results suggest that actomyosin activity not only permits the rapid adaptation of epithelia to compressive strain but also sets the buckling threshold, controlling the transition between planarity and folding in response to long-lasting compressive deformations.

Tissue pre-tension buffers against compression to prevent buckling

While buckling occurs under compressive stress in inert materials, epithelial tissues *in vivo* and *in vitro* are often actively pre-tensed by the actomyosin cytoskeleton[17,24,25]. We therefore hypothesised that actomyosin could tune the buckling threshold by controlling

the magnitude of pre-tension. To test this, we measured pre-stress in MDCK monolayers (Fig. 3a). We found that pre-stress in control conditions was tensional with a magnitude of 240 ± 30 Pa (Fig. 3b) - close to values measured via monolayer stress microscopy[26]. This pre-tension decreased dramatically with inhibition of contractility and increased when myosin activity was increased (Fig. 3b). Thus, pre-tension generation requires actomyosin and changes in the buckling threshold caused by actomyosin perturbation (Fig. 2e) were accompanied by changes in tissue pre-tension.

To characterise how tissue stress evolved during compressive strain, we applied a slow deformation to the tissues (as in Fig. 1f) whilst measuring the tissue-level tension (Fig. 3c and Methods). Tissue stress initially decreased linearly with strain, before transitioning, at a stress of 13 ± 4 Pa, to a second phase in which stress plateaued close to zero Pa (Fig. 3d, yellow). Such a stress-strain curve is a typical signature of a thin elastic sheet with a small bending modulus experiencing a buckling instability[27]. In support of this, the transition between the two phases occurred for a device strain of -33 ± 8 % (Fig. 3d, dashed line, and Fig. 3e), indistinguishable from the buckling threshold identified by imaging ($p = 0.53$, Fig. 3e). This transition point remained stable over multiple compression cycles (Supplementary Fig. 4a,b) and when several minutes of stretch preceded compression (Fig. 3d, orange). These data further suggest that the buckling threshold is an intrinsic mechanical feature of the tissue to which we can associate a reference length.

Next, we measured the evolution of tissue stress in response to rapid steps in compressive strain of various magnitudes (2-65%). Stress always decreased immediately upon application of compressive strain, however, for all but the largest strains, stress was rapidly re-established (Fig. 3f). Stress then plateaued at a level which depended on the

magnitude of compressive strain applied, with a larger fraction of the pre-tension recovered after smaller strains (Fig. 3f). The curve relating steady-state stress to strain magnitude in high strain rate experiments closely matched the stress response observed during slow strain application (compare Fig. 3g and 3d). Indeed, the fraction of recovered stress decreased linearly with increasing compressive strain up to a transition point at a device strain of ~-33%, below which there was no stress recovery (Fig. 3g).

Thus, the steady state stress in MDCK monolayers evolves linearly with compressive strain, independently of the history of deformation, and planar tissue morphologies can only be maintained when this steady state stress is tensional.

Epithelia behave as pre-tensed visco-elastic materials

These findings demonstrate that there exists a quasi-static regime in which the tissue behaves as a pre-tensed elastic sheet with negligible bending stiffness. Additionally, the time-scales of tissue flattening (Fig. 1) and tension recovery (Fig. 3) suggest that a viscous contribution damps the response. To test this, we devised a simple rheological model consisting of a standard linear solid (SLS, in line with [19]) in parallel with an active pre-tension element (Fig. 4a and Supplementary Information-Appendix 2). To account for the non-linearity at the buckling transition, in accordance with Euler buckling theory, we also supplemented the model with a 'buckling condition' in the form of a loss of tissue stiffness when stress becomes negative (Fig. 4a, Supplementary Information-Appendix 2A).

As observed in experiments, the assumptions of the model immediately imply that, upon application of compressive strain, the tissue may either buckle or remain planar, depending on the applied strain and strain rate (Supplementary Fig. 5a, Supplementary Information-Appendix 2F). For example, when deformation below the buckling threshold is

applied at sufficiently high strain rate, the tissue transiently buckles (as in Fig. 1b (i)). Indeed, under these conditions, the spring-dashpot element in the model behaves elastically at short time-scales and causes the tissue stress to transiently decrease to zero. Then, as the dashpot relaxes, stress recovers and the tissue flattens.

To test whether the behaviour of epithelia subjected to compressive strain can indeed be captured by such a mechanical model, we parametrised the model from experiments (Supplementary Information-Appendix 3) and simulated a set of mechanical perturbations. The parameters σ_a and E directly predict a buckling threshold $\varepsilon_b = -\sigma_a / E$ (Supplementary Information, Appendix 2). Indeed, at this strain, the elastic branch E is subjected to a stress equal to $-\sigma_a$, reducing stress to zero in the tissue. With E measured as 640 ± 80 Pa the ratio predicts a value of -38% for the buckling threshold, in close agreement with experiments (Fig. 1e and 3e). Furthermore, the model could accurately reproduce the temporal evolution of global tissue strain observed in experiments applying compressive strain at low strain rate (Fig 4b). Simulations also accurately captured the different regimes of stress recovery after a fast step of compression (Fig. 3f, Supplementary Fig. 5c and Supplementary Information-Appendix 2D), as well as the extent of this recovery as a function of applied compressive strain (Fig. 3g).

Epithelia possess short term memory of past compression

A further prediction of the model was that the time required for the tissue to flatten should depend on the history of deformation (Supplementary Information-Appendix 2E). To test this experimentally, three cycles of 40% compressive strain were applied to the tissue at high strain rate (Fig. 4c). After each 6-minute period of compressive strain, the tissue was returned to its original length for a chosen duration Δt (cycle 1: Δt_1 = 3s; cycle 2: Δt_2 = 6 min).

The tissues reached a planar configuration significantly faster after the second application of compressive strain compared with the first (Fig. 4d,e and Supplementary Video 8), confirming that the time necessary to flatten does depend on the tissue's history of deformation. This 'memory' was recapitulated in the model (Fig. 4e (ii)) and results from incomplete relaxation of the viscous element during the period Δt_1.

Conversely, after 6 minutes of rest at the initial length (Δt_2, Fig. 4c), which is predicted to be sufficient for full relaxation, the time required to become planar was indistinguishable from that during the first compressive period. This demonstrates that the 'memory' of the past compression was lost during Δt_2 (Fig. 4d,f and Supplementary Video 9).

Pre-tension and stiffness predict the buckling threshold

In our model, the buckling threshold of epithelia ε_b emerges as the ratio between their pre-tension σ_a and their long time-scale stiffness E. By modulating these parameters, epithelia may be able to regulate their buckling threshold to adapt to different developmental and physiological contexts.

To directly test this prediction, we performed experiments in which we altered the ratio between σ_a and E using inhibitors. Since our experiments indicated that both ε_b and σ_a are affected by regulators of contractility, we determined how E depended on actomyosin activity by subjecting MDCK epithelia to a ramp of compressive strain in their quasi-static elastic regime (as in Fig. 3d). The stress-strain curves of treated samples had the same form as controls, consisting of a first regime where stress was proportional to strain, followed by a saturation close to zero stress at high compressive strain (Fig. 5a). Treatments perturbing myosin activity led to changes in the stiffness E (30% decrease for

Y-27632 treatment and 60% increase for calyculin A, Fig. 5b and Supplementary Fig. 6a for paired comparisons) and to comparatively larger changes in pre-tension (45% decrease for Y-27632 and 75% increase for calyculin A, Fig. 3b and Supplementary Fig. 6b for paired comparisons). Thus changes in σ_a were dominant and the ratio σ_a / E was significantly modified (Fig. 5c). As predicted by our model, the buckling threshold was always very close to the ratio $-\sigma_a$ / E in all conditions even though this ratio was varied by a factor of ~10 across experimental conditions (Fig. 5d). Furthermore, when E and σ_a were decreased by a similar proportion by low dose latrunculin-B treatment (Fig. 5a-c), the buckling threshold only slightly decreased (Fig. 5a,d and Supplementary Fig. 6c).

Notably, variations in buckling threshold did not correlate with changes in the architecture of the inter-cellular junctions. High dose latrunculin-B treatment (1μM) led to disaggregation of the junctional network leaving only small remnants of junctional F-actin (Supplementary Fig. 6d), whereas Y-27632 did not affect junctional F-actin. However, both treatments caused a similar reduction in buckling threshold. Conversely, in Y-27632 and calyculin A treatments, the buckling threshold was altered in opposite directions without noticeable changes in cell-cell junctions (Supplementary Fig. 6d), suggesting that myosin II activity affects long term stiffness E indirectly by changing tension within the actin network. Overall, our data show that the ratio $-\sigma_a$ / E derived from our model matches the measured buckling threshold over a wide range of mechano-biological conditions. To provide a full understanding of the phenomenon from the molecular-scale up, future work will need to uncover the molecular pathways regulating tissue stiffness and pre-tension.

Outlook

Our results reveal that epithelia can accommodate remarkably large and rapid reductions in surface area. This response to compressive strains arises from isometric cell shape changes and is orchestrated autonomously by the actomyosin cytoskeleton, which not only controls the dynamics of the response but also the transition from planar to folded morphology. We observed identical behaviours in epithelia from different tissues (kidney and skin) and with different organisations (mono- and multi-layered). The full range of behaviours observed could be reproduced by a simple zero-dimensional mechanical model of the epithelium as a pre-tensed visco-elastic sheet that exhibits a buckling instability upon reaching compressive stress. Based on this model, we propose that the visco-elastic properties of the tissue set the time-scale of the cell shape adaptation that enables flattening. This time-scale – on the order of tens of seconds – is commensurate with that of mechanical relaxation observed in Drosophila[18, 29,30], with the relaxation of stress fibres following nanosurgery[31] and with the turnover rate of the proteins of the actomyosin cytoskeleton[32].

Our results demonstrate that the tissue response possesses a well-defined limit at a compressive strain of ~35%, i.e. the buckling threshold, above which stable folds can be formed. The close match between the buckling threshold of MDCK and HaCaT epithelia suggests that it is not a tissue-specific property but rather may stem from the bulk properties of actomyosin networks. Indeed, the buckling threshold is regulated by the interplay between myosin generated pre-tension and tissue elasticity – the ratio of these two quantities defines the strain at which the tissue reaches compressive stress. Although our experiments only consider epithelia devoid of a substrate, our model indicates that the buckling threshold should only be marginally modified by the presence of a thin extra-cellular matrix such as found in the lung[33] or many developing tissues undergoing morphogenesis[34,35] (Supplementary Information-Appendix 4). The buckling instability

which we uncover may act in parallel to other well-studied mechanisms of epithelial bending and folding, which include differential growth of connected tissues[7,36] and spatially patterned force generation[37]. Indeed, apical (or basal) constrictions are often preceded *in vivo* by an increase in cell density before fold formation[2,6], implying that polarized constriction is accompanied by a planar compressive deformation of cells, which could tune tissue folding. Thus, future studies should consider a role for the reduction of tissue pre-tension during epithelial folding.

Together, the buckling threshold and flattening time-scale define the maximum strain and strain rate that can be imposed upon an epithelium before it becomes subjected to compressive stresses. Such stresses can be damaging to cells[38] and stress accumulation at the epithelium-substrate interface could lead to delamination of the epithelium. The buckling threshold and flattening time-scale are therefore crucial material parameters for understanding the response of epithelia to compressive strain during morphogenesis or normal organ physiology. On longer time-scales, this underlines the need for cellular-scale mechanisms such as cell delamination in epithelia to counter the deleterious effects of prolonged compression[13,14]. Finally, our results also raise the possibility that actomyosin pre-tension may play a role in various cell[39,40] and tissue contexts throughout evolution to act as a buffer against unwanted stresses and distortions of shape that may otherwise be caused by compression.

References

1. Tschumperlin, D. J., *et al*. Bronchial epithelial compression regulates MAP kinase signaling and HB-EGF-like growth factor expression, *American Journal of Physiology-Lung Cellular and Molecular Physiology* **282**, L904-L911 (2002).

2. Martin, A. C., Kaschube, M. & Wieschaus, E. F. Pulsed contractions of an actin–myosin network drive apical constriction. *Nature* **457,** 495–499 (2009).

3. Shyer, A. E. *et al.* Emergent cellular self-organization and mechanosensation initiate follicle pattern in the avian skin, *Science* **357**, 811-815 (2017).

4. Etournay, R. *et al.* Interplay of cell dynamics and epithelial tension during morphogenesis of the Drosophila pupal wing, *eLife* **4,** (2015).

5. Brodland, G. W. *et al.* Video force microscopy reveals the mechanics of ventral furrow invagination in Drosophila. *Proc. Natl. Acad. Sci. USA* **107,** 22111–22116 (2010).

6. Sidhaye, J. & Norden, C. Concerted action of neuroepithelial basal shrinkage and active epithelial migration ensures efficient optic cup morphogenesis. *Elife* **6,** 1–29 (2017).

7. Shyer, A. E. *et al.* Villification: How the Gut Gets Its Villi, *Science* **342,** 212-218 (2013).

8. Park, J.-A. *et al.* Unjamming and cell shape in the asthmatic airway epithelium. *Nat. Mater.* **14,** 1040–1048 (2015).

9. Grainge, C. L. *et al.* Effect of Bronchoconstriction on Airway Remodeling in Asthma. *N. Engl. J. Med.* **364,** 2006–2015 (2011).

10. Tallinen, T. *et al.* On the growth and form of cortical convolutions. *Nat. Phys.* **12,** 588–593 (2016).

11. Aragona, M. *et al.* A mechanical checkpoint controls multicellular growth through YAP/TAZ regulation by actin-processing factors. *Cell* **154,** 1047-1049 (2013).

12. Desprat, N., Supatto, W., Pouille, P. A., Beaurepaire, E. & Farge, E. Tissue Deformation Modulates Twist Expression to Determine Anterior Midgut Differentiation in Drosophila Embryos. *Dev. Cell* **15,** 470–477 (2008).

13. Eisenhoffer, G. T. *et al.* Crowding induces live cell extrusion to maintain homeostatic cell numbers in epithelia. *Nature* **484,** 546–549 (2012).

14. Marinari, E. *et al.* Live-cell delamination counterbalances epithelial growth to limit tissue overcrowding. *Nature* **484,** 542–545 (2012).

15. Wyatt, T., Baum, B. & Charras, G. A question of time: Tissue adaptation to mechanical forces. *Curr. Opin. Cell Biol.* **38,** 68–73 (2016).

16. Étienne, J. *et al.* Cells as liquid motors: Mechanosensitivity emerges from collective dynamics of actomyosin cortex. *Proc. Natl. Acad. Sci. USA* **112 (9),** 2740–2745 (2015).

17. Chanet, S. *et al.* Actomyosin meshwork mechanosensing enables tissue shape to orient cell force. *Nat. Commun.* **8,** 1–13 (2017).

18. Clément, R., Collinet, C., Dehapiot, B., Lecuit, T. & Lenne, P. Viscoelastic dissipation stabilizes cell shape changes during tissue morphogenesis. *Current Biology* **27,** 3132–3142 (2017).

19. Harris, A. R. *et al.* Characterizing the mechanics of cultured cell monolayers. *Proc. Natl. Acad. Sci. USA* **109,** 16449–16454 (2012).

20. Harris, A. R. *et al.* Generating suspended cell monolayers for mechanobiological studies. *Nat. Protoc.* **8,** (2013).

21. Wyatt, T. P. J. *et al.* Emergence of homeostatic epithelial packing and stress dissipation through divisions oriented along the long cell axis. *Proc. Natl. Acad. Sci. USA* **112,** 5726–5731 (2015).

22. Salbreux, G., Charras, G. & Paluch, E. Actin cortex mechanics and cellular morphogenesis. *Trends Cell Biol.* **22,** 536–545 (2012).

23. Fischer-Friedrich, E. *et al.* Rheology of the Active Cell Cortex in Mitosis. *Biophys. J.* **111,** 589–600 (2016).

24. Hutson, M. S. *et al.* Forces for morphogenesis investigated with laser microsurgery and quantitative modeling. *Science* **300,** 145–149 (2003).

25. Valon, L., Marín-Llauradó, A., Wyatt, T., Charras, G. & Trepat, X. Optogenetic control of cellular forces and mechanotransduction. *Nat. Commun.* **8,** 14396 (2017).

26. Tambe, D. T. *et al.* Collective cell guidance by cooperative intercellular forces. *Nat. Mater.* **10,** 469–475 (2011).

27. Audoly, B. & Pomeau, Y. *Elasticity and Geometry*. *From hair curls to the non-linear response of shells,* (Ed.) Oxford University Press.

28. Vishwakarma, M. *et al.* Mechanical interactions among followers determine the emergence of leaders in migrating epithelial cell collectives. *Nat. Commun.* **9,** (2018).

29. Bonnet, I. *et al.* Mechanical state, material properties and continuous description of an epithelial tissue. *J. R. Soc. Interface* **9,** 2614–2623 (2012).

30. Bambardekar, K., Clément, R., Blanc, O., Chardès, C. & Lenne, P.-F. Direct laser manipulation reveals the mechanics of cell contacts in vivo. *Proc. Natl. Acad. Sci. USA* **112,** 1416–1421 (2015).

31. Kassianidou, E., Brand, C. A., Schwarz, U. S. & Kumar, S. Geometry and network connectivity govern the mechanics of stress fibers. *Proc. Natl. Acad. Sci. USA* (2017). doi:10.1073/pnas.1606649114

32. Khalilgharibi, N., Fouchard, J., Recho, P., Charras, G. & Kabla, A. The dynamic mechanical properties of cellularised aggregates. *Curr. Opin. Cell Biol.* **42,** (2016).

33. Weibel, E. R. On the tricks alveolar epithelial cells play to make a good lung. *Am. J. Respir. Crit. Care Med.* **191,** 504–513 (2015).

34. Pastor-Pareja, J. C. & Xu, T. Shaping Cells and Organs in Drosophila by Opposing Roles of Fat Body-Secreted Collagen IV and Perlecan. *Dev. Cell* (2011).

35. Davidson, L. A., Keller, R. & DeSimone, D. W. Assembly and remodeling of the fibrillar fibronectin extracellular matrix during gastrulation and neurulation in Xenopus laevis. *Dev. Dyn.* (2004).

36. Nelson, C. M. On Buckling Morphogenesis. *J. Biomech. Eng.* **138,** 021005 (2016).

37. Lecuit, T. & Lenne, P.-F. Cell surface mechanics and the control of cell shape, tissue patterns and morphogenesis. *Nat. Rev. Mol. Cell Biol.* **8,** 633–644 (2007).

38. Kocgozlu, L. *et al.* Epithelial Cell Packing Induces Distinct Modes of Cell Extrusions. *Curr. Biol.* **26,** 2942–2950 (2016).

39. Costa, K. D., Hucker, W. J. & Yin, F. C. P. Buckling of actin stress fibers: A new wrinkle in the cytoskeletal tapestry. *Cell Motil. Cytoskeleton* **52,** 266–274 (2002).

40. Tofangchi, A., Fan, A. & Saif, M. T. A. Mechanism of Axonal Contractility in Embryonic Drosophila Motor Neurons In Vivo. *Biophys. J.* **111,** 1519–1527 (2016).

Acknowledgements

The authors wish to acknowledge past and present members of the Charras, Baum, and Kabla labs for stimulating discussions as well as Duncan Farquharson and Simon Townsend at the UCL workshop and Ys. T.W. and N.K. were part of the EPSRC funded doctoral training program CoMPLEX. J.F. and P.R. were funded by BBSRC grant (BB/M003280 and BB/M002578) to G.C. and A.K. N.K. was funded by the Rosetrees Trust and the UCL Graduate School through a UCL Overseas Research Scholarship. A.L. was supported by an EMBO long term post-doctoral fellowship. B.B. was supported by UCL, a BBSRC project grant (BB/K009001/1) and a CRUK programme grant (17343). T.W., J.F., N.K., A.L. and G.C. were supported by a consolidator grant from the European Research Council to G.C. (MolCellTissMech, agreement 647186).

Author contributions

T.W., J.F., B.B. and G.C. designed the experiments. T.W., J.F., A.L., and N.K. carried out the experiments. T.W. and J.F. performed the data and image analysis. P.R. and A.K. designed the rheological model. T.W., J.F., B.B. and G.C. wrote the manuscript. All authors discussed the results and manuscript.

Competing financial interests

The authors declare no competing financial interests.

Data availability statement

The data that support the findings of this study are available from the corresponding authors upon reasonable request.

Code availability statement

All code created for the analysis of the data in this study is available from the corresponding authors upon reasonable request.

Methods

Cell Culture

MDCK and HaCaT cells were cultured at 37°C in an atmosphere of 5% CO_2. Cells were passaged at a 1:5 ratio every 3-4 days using standard cell culture protocols and disposed of after 30 passages. For MDCK cells, the culture medium was composed of high glucose DMEM (Thermo Fisher Scientific) supplemented with 10% FBS (Sigma) and 1% penicillin-streptomycin (Thermo Fisher Scientific). MDCK-E-Cadherin-GFP cell lines (generated as described in [20]) were cultured in the same conditions as wild-type cells except that 250 ng/ml puromycin was added to the culture medium. HaCaT cells were cultured in low calcium conditions, consisting of a minimal DMEM supplemented with 0.03 mM $CaCl_2$, 10% calcium-free FBS, 1% penicillin-streptomycin and 1% L-Glutamine (Gibco).

Fabrication of devices for imaging of tissue response to compression and for stress measurement during compression

For profile imaging of epithelia during compression, tissues were cultured on custom made imaging devices as described in [21]. Briefly, device arms were made from glass capillaries (Sutter Instruments) and a length of nickel-titanium (nitinol) wire (Euroflex) that acted as a hinge. Glass coverslips (VWR) were glued to the glass capillaries to act as a substrate for cell culture. To allow precise control over both compressive and tensile strains, another small piece of glass capillary was added to the hinged side of the device at an angle to allow continuous contact with the micro-manipulator probe (see illustration in Fig. 1a).

The stress measurement devices were an adaptation of the force measurement device described in [20]. Briefly, a nickel-titanium (nitinol) wire the wire was glued into a bent glass capillary. Then, tygon cylinders were glued to the extremities of the capillary and wire. A

hinge was added at the base of the rigid rod to control the applied deformation via a motorised micromanipulator while the force was computed from images of the movement of the flexible wire and the stiffness of the flexible wire (see illustration in Fig. 3a).

Generation of suspended tissues and preconditioning

Suspended monolayers of MDCK cells were generated as described in [19]. Briefly, a drop of collagen was placed between the test rods and left to dry at 37°C to form a solid scaffold. This collagen was then rehydrated before cells were seeded onto it and cultured for 48-72 hours. Immediately before each experiment the collagen scaffold was removed via enzymatic digestion. HaCaT epithelia were made using the same procedure. During the generation of HaCaT epithelia, cells were grown in high calcium culture medium instead of the low calcium medium used for routine culture to allow the formation of robust intercellular junctions.

Before each experiment, the tissues were preconditioned by applying 5 cycles of 30% stretch at a rate of 1 $\%.s^{-1}$. The tissues were then left unperturbed for 6 minutes before application of compressive strain.

Confocal imaging of tissues and mechanical manipulation

Tissues were imaged at 37°C in a humidified atmosphere with 5% CO_2. The imaging medium consisted of DMEM without phenol red supplemented with 10% FBS. To visualise the shape of the tissue during mechanical manipulation, cell membranes were labelled with CellMask membrane stain for 10 minutes following the manufacturer protocol (Thermo Fisher Scientific). AlexaFluor-647-conjugated dextran, 10,000 MW (Thermo Fisher Scientific) was added at 20 $\mu g.mL^{-1}$ to the imaging medium to visualise by exclusion the coverslips on which the epithelia were grown.

Profile views of the tissues during mechanical manipulation were obtained using a 30X objective (UPLSAPO S, NA=1.05, Olympus) mounted on an Olympus IX83 inverted microscope equipped with a scanning laser confocal head (Olympus FV1200). Each image consisted of approximately 200 slices spaced by 0.5 μm. Time series were acquired with an interval of ~2 seconds between frames.

For imaging of cell shape change, cell membranes were visualized with CellMask. Z-stacks were acquired using a 60X objective (UPLSAPO, NA=1.3, Olympus) mounted on a spinning disk confocal microscope which consisted of a Yokogawa spinning disk head (CSU22; Yokogawa) and an iXon camera (Andor) interfaced to an IX81 Olympus inverted microscope.

To apply the mechanical deformation during confocal imaging, a custom-made adaptor was wedged in the top end of the hinged arm of the stretching device. The adaptor was connected to a 2-D manual micromanipulator mounted on a motorized platform (M-126.DG1 controlled through a C-863 controller, Physik Instrumente). The manual micromanipulators were used for initial positioning of the adaptor. Then, the tissues were deformed by moving the motorized platform which was controlled via a custom-made Labview program (National Instruments).

Quantification of device strain, tissue strain and flattening half-life

To precisely quantify the imposed compressive strain, the positions of the two coverslip edges which delimited the span of suspended tissue were determined by segmentation of dye exclusion in Alexa-647 fluorescence images. The strain imposed by the device was then defined as:

$$\varepsilon_d = \frac{d - l_0}{l_0} \quad (1)$$

where l_0 and d are the coverslip-to-coverslip distances before and after compressive strain, respectively.

To quantify length evolution in images of tissue profiles in response to compression, an implementation of the Chan-Vese algorithm[41] in Mathematica (Wolfram Research) was used to segment the cells from the background. To convert each binary mask generated by segmentation into a line, morphological thinning was applied to the mask repeatedly until complete skeletonisation. The length of the shortest path between opposite edges of the image via foreground pixels thus constituted a measure of the cross-sectional contour length of the epithelia (see Supplementary Fig. 1b). The tissue strain at each time point was then defined as:

$$\varepsilon(t) = \frac{l(t) - l_0}{l_0} \quad (2)$$

where l_0 and $l(t)$ are the suspended tissue length before deformation and at time t after application of compressive strain, respectively.

The half-life of tissue strain in response to a step of compression (Fig. 1) was defined as the time necessary for the tissue to decrease its contour length by 50% of the total length change that occurred. This time was extracted after polynomial interpolation of the evolution of tissue strain with time $\varepsilon(t)$.

Quantification of 3D cell shapes

The cell outlines were automatically segmented using the Fiji[42] plugin *Tissue Analyzer*[43]. Segmentation was subsequently verified and corrected manually if necessary. Measurements of cell shape were extracted from the resulting outlines using custom written routines in Mathematica (Wolfram Research). Cell length measurements were obtained by calculating the minimum bounding box of the cell outline. Bounding boxes were oriented along the experimental x- and y-axes with the x-axis corresponding to the axis of deformation. Measurements of cell height were obtained manually in Fiji from cross-sectional slices through the image stack along y-z planes.

Drug treatments

Drug treatments were performed as follows. To block myosin contractility, blebbistatin was added at a 20 μM concentration for MDCK tissues or 75 μM concentration for HaCaT tissues, 10 minutes prior to experiments. To block Rho-kinase activity, Y-27632 was added at a concentration of 20 μM, 10 minutes prior to experiments. To increase myosin contractility, phosphatases were inhibited by addition of 35 nM of calyculin A 10 minutes prior to experiments. For complete depolymerisation of the F-actin cytoskeleton, we treated tissues with 3 μM latrunculin-B for 30 minutes prior to experiments. For dose-dependent depolymerisation of junctional F-actin, we treated tissues with either 1 μM or 0.1 μM latrunculin-B for 1 hour prior to experiments.

Mechanical testing experiments

Mechanical testing experiments were performed at 37°C in Leibovitz's L15 without phenol red (Thermo Fisher Scientific) supplemented with 10% FBS. Tissues were imaged every second using a 2X objective (2X PLN, Olympus) mounted on an inverted microscope (Olympus IX-71). Images were acquired with a CCD camera (GS3-U3-60QS6M-C, Pointgrey). Compressive strain was applied using the motorized platform described above.

606

607 **Stress-strain measurements**

608 To measure the uni-axial stress in the tissue, we measured the deflection of the flexible
609 arm of the device from images before and after detachment of the tissue (see Fig. 3a). The
610 epithelia were detached from the reference arm of the device by cutting them with a
611 tungsten needle.

612

613 The force applied by the tissue on the flexible arm can be estimated by considering that
614 the flexible arm acts as a cantilevered beam. We define x_i^w as the position of the wire
615 when the epithelium is attached between the bars and x_0^w as the position of the wire when
616 the epithelium is detached from the bars (the rest position). The force applied by the tissue
617 on the wire is given by:

$$F = k\Delta x^w = k(x_i^w - x_0^w) \quad (3)$$

618 where k is the stiffness of the wire defined as:

$$k = \frac{3\pi E r^4}{4L^3} \quad (4)$$

619 Here, E is the Young's modulus of the wire, r its radius, and L its length. E was
620 independently measured by loading the wire with pieces of plasticine of different weights
621 and measuring the deflection of the wire as described in[20].

622

623 The stress in the tissue was then computed as:

$$\sigma = \frac{F}{wh} \quad (5)$$

624 Where w is the average width of the tissue determined from bright field images and h the
625 tissue thickness. As shown in Figure 2a-b, tissue thickness was dependent on the applied
626 strain. Previous work[19] and Figure 2b show that the cell volume remains constant during
627 changes in tissue area. However, once the buckling threshold ($\varepsilon_b \sim -0.35$) is exceeded, the
628 tissue length does not change and therefore the thickness also does not change. With

these assumptions, we could estimate the evolution of the thickness h for calculation of σ as follows:

$$h_{[\varepsilon>-0.4]} = \frac{h_0}{1+\varepsilon} \tag{6}$$

and

$$h_{[\varepsilon\leq-0.4]} = \frac{h_0}{1+\varepsilon_{[h=-0.4]}} \tag{7}$$

In experiments, the deflection of the wire Δx^w was determined by image cross-correlation with a sub-pixel accuracy through a custom-written algorithm based on the *register_translation* function of scikit-image, a Python image processing toolbox[44]. For the analysis, a portion of the wire was cropped from the images acquired during the experiments. The average error of the stress measurement method was measured from simulated displacements of the cropped region over 10 different samples. The deflection obtained via the algorithm was then compared to the deflection applied numerically. The difference found in force was 22 ± 31 nN (mean ± SD) which corresponds to 1.1 ± 1.6 Pa (mean ± SD).

Tissue pre-stress measurements (σ_a) were then obtained from the stress value before any deformation was imposed to the tissue, i.e. $\sigma = \frac{F}{wh}$.

For experiments in which tissue strain was varied, the position of the rigid rod $x^b(t)$ was used to compute the displacement applied to the tissue and the flexible rod was used to determine the stress in the epithelium. This position was extracted using the same method as for estimating the position of the flexible wire in pre-tension measurements (see above). The device strain was defined as:

$$\varepsilon = \frac{\Delta x^b + \Delta x^w}{l_0} \quad (8)$$

where $\Delta x^b = x_i^b - x_0^b$ refers to the displacement of the rigid rod, $\Delta x^w = x_i^w - x_0^w$ is the displacement of the flexible rod and l_0 is the initial rod-to-rod distance.

Note that the deflection of the flexible wire Δx^w due to the evolution of tissue stress over time was small compared to the deflection imposed by the movement of the rigid bar Δx^b. For example, for a dataset where a deformation of -54 ± 5% was applied, the movement of the wire led to a variation in deformation of only 6 ± 4% over the course of the experiment.

Determination of the buckling threshold from stress-strain curves

Stress-strain curves were biphasic with stress first decreasing linearly with strain before saturating at high compressive strain. The transition strain between the two regimes was determined as follows. For each strain ε_i between [0, ε_{max}], we fitted a linear function to the stress σ over the interval [0, ε_i] and a constant over the interval [ε_i,ε_{max}]. For each ε_i, the average of the sum of residuals is computed:

$$R_{[0,\varepsilon_i]} = \frac{1}{N}\sum_{i=1}^{N}\left(\Delta R^2 - (a\varepsilon_i + b)\right)^2 \quad (9)$$

and

$$R_{[\varepsilon_i,\varepsilon_{max}]} = \frac{1}{N}\sum_{i=1}^{N}(\Delta R^2 - b)^2 \quad (10)$$

The transition point is then defined as the strain ε_i which minimizes the sum of the average errors over each interval:

$$R_{tot}(\varepsilon_t) = min\left(R_{[0,\varepsilon_i]} + R_{[\varepsilon_i,\varepsilon_{max}]}\right) \quad (11)$$

The stress at transition was then equal to $\sigma_t = \sigma(\varepsilon_t)$. In addition, the elasticity of the tissue E could be extracted from the slope of the linear portion of curve.

F-actin staining

MDCK Ecadherin-GFP cells were cultured to 90% confluence on glass coverslips. They were fixed with 4% paraformaldehyde diluted in PBS for 20 minutes at room temperature, permeabilised in 0.2% Triton-X in PBS for 5 min and blocked with a solution of 10% horse serum in PBS for 30 min. To label F-actin, the cells were incubated with a solution of Phalloidin-Alexa-647 diluted at 1:40 from a stock solution of 200 units.mL^{-1} for 1 hour at room temperature. The samples were then imaged on an Olympus FV-1200 confocal microscope.

Other statistical and data analysis

All other routine data and statistical analyses were performed using the Python language environment and its scientific libraries (NumPy, SciPy) as well as Mathematica. Image processing was carried out with the Fiji package. All boxplots show the median value (central bar), the first and third quartile (bounding box) and the range (whiskers) of the distribution. All tests of statistical significance are Mann-Whitney U tests, or Wilcoxon signed-rank tests for paired tests, unless otherwise stated. Measured values are given as mean ± standard error unless otherwise stated. Each dataset is pooled across experiments which were performed on at least 3 separate days. In all boxplots, * denotes statistically significant difference, $p < 0.05$, ** denotes $p < 0.01$ and *** denotes $p < 0.001$. The number of tissues examined in each condition is indicated above each boxplot.

References

41. Chan, T. F. and Vese, L. A. Active contours without edges, *IEEE Transactions on Image Processing* **10,** 266-277 (2001).

42. Schindelin, *et al.* Fiji: an open-source platform for biological-image analysis, *Nat Meth* **9,** 676-682 (2012).

43. Aigouy, B., *et al.* Cell Flow Reorients the Axis of Planar Polarity in the Wing Epithelium of Drosophila, *Cell* **142,** 773 - 786 (2010).

44. van der Walt, *et al.* scikit-image: image processing in Python, *PeerJ* **2,** e453 (2014).

Figure legends

Figure 1.

Fast mechanical adaptation of epithelia to compression. **a**, Schematic diagram showing the method for application of compressive strain to suspended epithelia. *i:* Top view of the mechanical manipulation device. Uniaxial strain is applied to the tissue (green) by displacing the flexible arm. *ii-iii:* profile views of the setup along the dashed line in *i*. *ii:* An epithelium (green) is suspended between two coverslips (black). *iii:* the right-hand coverslip is displaced, deforming the tissue. The yellow line denotes the distance between the coverslips from which the applied 'device strain' is calculated. The blue dotted line denotes the tissue contour length. **b**, Time series of profiles of epithelia before and during application of various compressive strains ε, applied at different rates. Strain was applied either as a step at high strain rate (500 $\%.s^{-1}$, *i-ii and iv-v*) or as a ramp at low strain rate (0.5 $\%.s^{-1}$, *iii and vi*). *i*: Step of intermediate amplitude (-35%), *ii*: step of large amplitude (-50%) and *iii*: strain ramp (-80%), applied to MDCK monolayers. *iv-vi:* As in *i-iii* but for multi-layered HaCaT epithelia. Cell membranes are marked with CellMask (green), the medium is visualised by addition of dextran Alexa-647 (red) making coverslips appear dark due to dye exclusion. Scale bars, 20 μm. **c**, Temporal evolution of the tissue strain (blue) of an MDCK monolayer resulting from a step of -35% device strain (yellow) and **d**, -50% device strain. **e**, Comparison of the buckling threshold ε_b in MDCK and HaCaT epithelia measured following a fast step or a slow ramp of compressive strain. The number of tissues examined is indicated above each boxplot. n.s. = not significant. **f**, Temporal evolution of the tissue strain (blue) during a ramp of device strain (yellow). The dashed lines in (**d**,**f**) mark the maximum tissue strain, termed the buckling threshold ε_b.

Figure 2.

Tissue flattening is achieved through myosin-dependent cell shape change. **a**, Confocal images of MDCK epithelial monolayers before (left) and during (right) 30% uniaxial compressive strain. Plasma membranes are marked with CellMask (green) and nuclei with Hoechst-33342 (red). Top: Single x-y confocal optical section through the middle of the tissue. Bottom: y-z profile. Compressive strain is applied along the x-axis. Scale bars, 10 μm. **b**, Cellular strain as a function of the strain applied to MDCK tissues. Solid circles denote cellular strain along the x-axis (red), y-axis (green), and z-axis (blue). Error bars denote standard deviation. Dashed lines indicate the predicted cellular strain assuming that cell strain accounts entirely for tissue strain and that cells maintain constant volume during deformation by increasing their height (z). **c**, Profile of *i*: an MDCK monolayer and *ii*: a HaCaT epithelium treated with blebbistatin (20 μM and 75μM, respectively) and subjected to fast compressive strain. Scale bars, 20 μm. Time is indicated in the top right-hand corner. **d**, Temporal evolution of tissue strain (mean ± SD) following fast compression for control (blue), blebbistatin (20 μM, red) and calyculin A (35 nM, purple) treated MDCK tissues. The number of epithelia examined for each condition is indicated in the figure inset. **e**, Buckling threshold ε_b inferred from the maximal tissue strain reached after fast compression of MDCK and HaCaT epithelia. Tissues were treated with drugs altering actomyosin contractility. Caly = calyculin A (35 nM); Bleb = blebbistatin (20 μM for MDCK, 75 μM for HaCaT); Y27 = Y-27632 (10 μM); Lat-B = latrunculin-B (3 μM). The number of tissues examined is indicated above each boxplot.

Figure 3.

Pre-tension buffers against compression to prevent stable buckling of epithelia. a, Schematic diagram depicting the principle of measurement of tissue pre-stress. Left: The tissue (green) is cultured between a reference rod and a flexible rod. Right: Measurement of the deflection of the flexible rod compared to its rest position allows determination of the

stress applied by the epithelium. The deflection of the flexible rod δ is measured from brightfield images acquired before and after detachment of the tissue. **b**, Pre-tension of MDCK monolayers treated with drugs altering actomyosin contractility. Caly = calyculin A (35 nM); Bleb = blebbistatin (50 μM); Y27 = Y-27632 (20 μM); Lat-B = latrunculin-B (3 μM). **c**, Schematic diagram for measurement of stress during application of compressive strain. The device is the same as in (**a**) but uniaxial strain is applied by displacing the left arm with a micromanipulator. **d**, Tissue stress as a function of applied device strain during deformation at low strain rate (0.5 %.s^{-1}). Different colours indicate different loading and unloading periods. The dashed line indicates the buckling threshold ε_b. Inset: Time course of the device strain applied. **e**, Comparison of the buckling threshold measured from the transition identified in stress-strain curves and from the maximum tissue strain identified during imaging experiments (Fig. 1e). n.s. = not significant. **f**, Representative temporal evolution of stress after application of compressive strains of various amplitudes ε_d applied at high strain rate (100 %.s^{-1}). The stress is normalised to the pre-tension in the tissue before deformation. **g**, Fraction of stress recovery at steady state as a function of device strain for deformation applied at high strain rate. The green line shows the behaviour predicted by the rheological model presented in Fig. 4a. (**b, e**) The number of tissues examined is indicated above each boxplot.

Figure 4.

Epithelia behave as a pre-tensed visco-elastic material. a, Diagram of the rheological model describing the mechanical response of epithelia to compression. An active element models the contractile stress (σ_a) generated by myosin II. The middle spring (of stiffness E) models the elastic behaviour of the tissue at long time-scales, while the spring-dashpot element (of stiffness Y and viscosity η) models the short time-scale elastic behaviour and viscous relaxation. A condition of loss of stiffness is added in series (left) to model the

buckling instability: when the material reaches zero-stress, its stiffness becomes null. **b**, Temporal evolution of tissue strain in response to slow cycles of compressive strain (80% amplitude applied at 0.5 $\%.s^{-1}$, yellow). Left: representative experimental dataset. Right: model prediction. **c**, Sequence of device strain applied to the tissues to assess dependence of the response on strain history. Three cycles of 40% compressive strain were applied, each lasting 6 minutes. After each cycle the tissue was returned to its original length for a duration Δt_1 = 3s (between cycles 1 and 2) and Δt_2 = 6 min (between cycles 2 and 3). **d**, Profile images of MDCK monolayers shown 2 seconds and 15 seconds after compressive strain application in each of the cycles. For each time point, the dashed white line corresponds to the maximal vertical deflection of the tissue during the first cycle. Scale bars, 20 μm. **e**, Temporal evolution of the tissue strain (mean ± SD) after the first (blue) and second (green) cycle of compressive strain (yellow). *i*: Experimental data, n = 12 tissues. *ii*: Model prediction. **f**, The same as (**e**) but for the first (blue) and third (purple) cycle of compressive strain.

Figure 5.

Pre-tension and stiffness predict the buckling threshold. **a**, Tissue stress measured as a function of applied compressive strain for low strain rate (mean ± SE). Control tissues are shown in blue, tissues treated with 0.1 μM latrunculin-B in purple, 1 μM latrunculin-B in red, 20 μM Y-27632 in yellow and 35 nM calyculin A in black. Note that the strain rate was chosen to ensure that all samples are tested in a quasi-static regime. The number of epithelia examined for each condition is indicated in the figure inset. **b**, Young's modulus E (as a measure of long time-scale stiffness) of the tissues for the same samples as in (**a**). Young's modulus was measured from the slope of the curve in (**a**) before transition to buckling. The horizontal grey line shows the median value for control tissues. **c,** Ratio $-\sigma_a$ / E corresponding to the buckling threshold predicted by our model for the same samples as

in (**a**). The horizontal grey line shows the median value for control tissues. **d**, Buckling threshold measured from the transition in the stress-strain curve as a function of the ratio - σ_a / E corresponding to the buckling threshold predicted by the model for all control and treated samples as in (**a**). The dashed line indicates the line along which these values match.

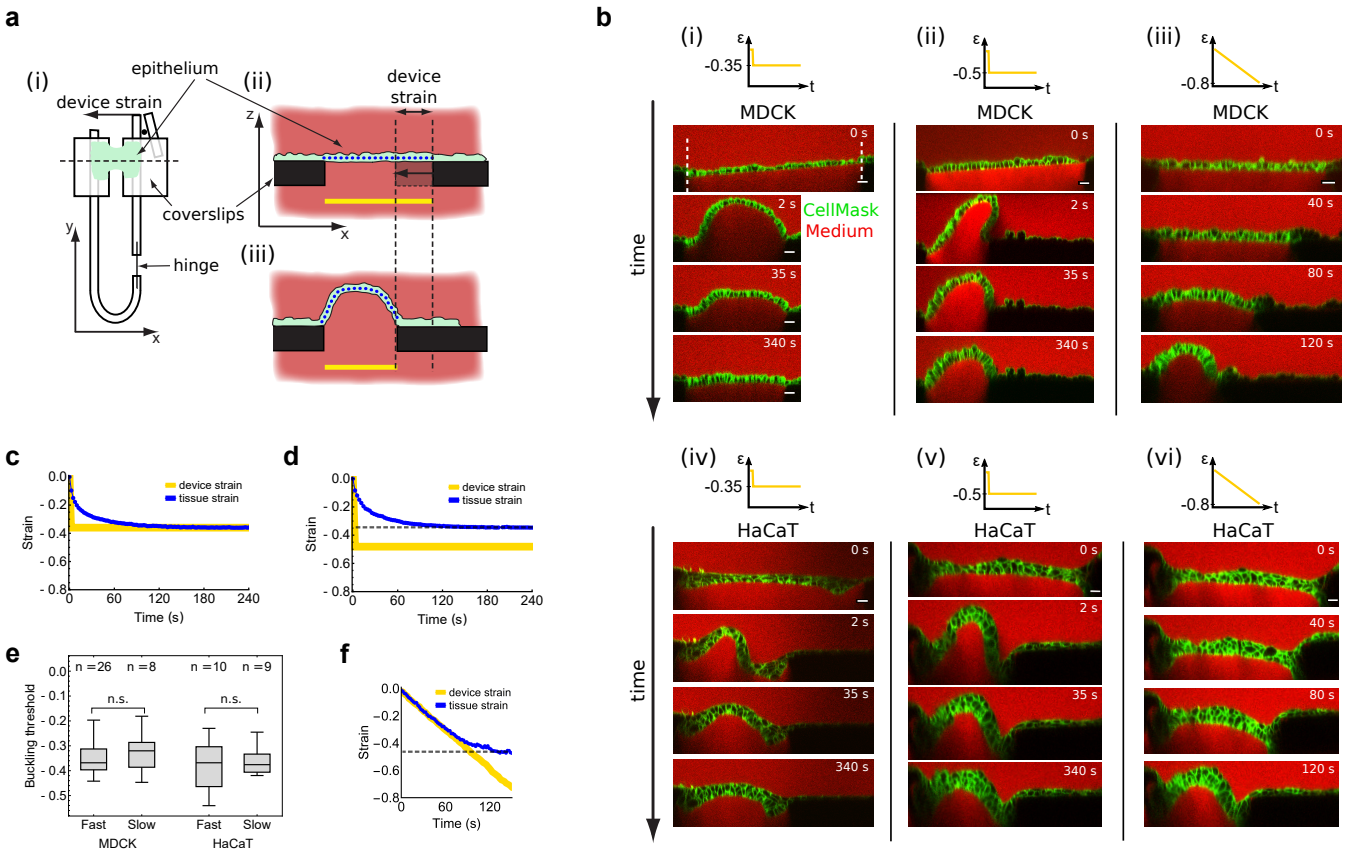
a
(i)
epithelium
device strain
coverslips
hinge
y
x
(ii)
device strain
z
x
(iii)
b
(i)
(ii)
(iii)
ε
-0.35
-0.5
-0.8
t
MDCK
time
0 s
2 s
35 s
340 s
CellMask
Medium
40 s
80 s
120 s
(iv)
(v)
(vi)
HaCaT
c
d
device strain
tissue strain
Strain
Time (s)
e
Buckling threshold
n =26
n =8
n =10
n =9
n.s.
Fast
Slow
MDCK
HaCaT
f

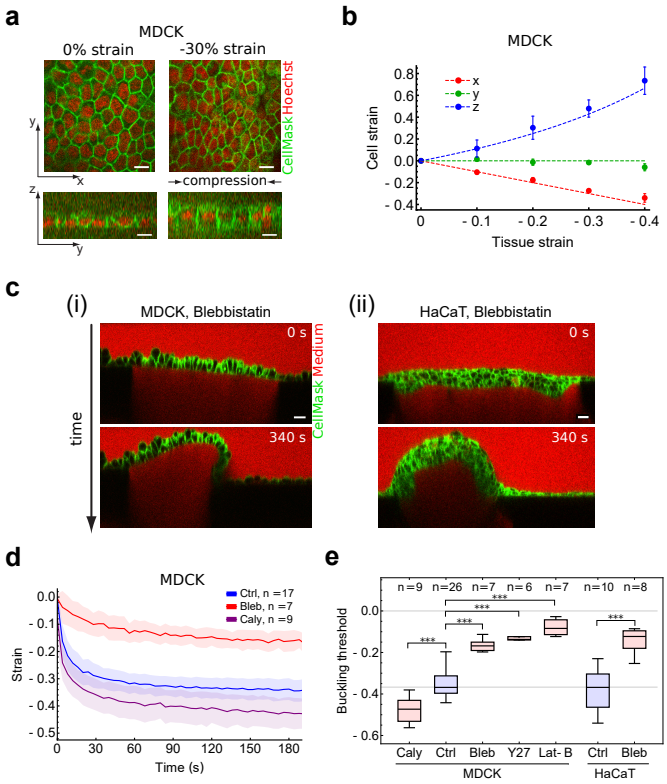
a
MDCK
0% strain
-30% strain
CellMask Hoechst
y
x
z
y
compression
b
MDCK
Cell strain
x
y
z
0.8
0.6
0.4
0.2
0.0
- 0.2
- 0.4
0
- 0.1
- 0.2
- 0.3
- 0.4
Tissue strain
c
(i)
MDCK, Blebbistatin
0 s
340 s
time
CellMask Medium
(ii)
HaCaT, Blebbistatin
0 s
340 s
d
MDCK
Ctrl, n =17
Bleb, n =7
Caly, n =9
Strain
0.0
- 0.1
- 0.2
- 0.3
- 0.4
- 0.5
0
30
60
90
120
150
180
Time (s)
e
n=9
n=26
n=7
n=6
n=7
n=10
n=8
***
Buckling threshold
0.0
- 0.2
- 0.4
- 0.6
Caly
Ctrl
Bleb
Y27
Lat- B
Ctrl
Bleb
MDCK
HaCaT

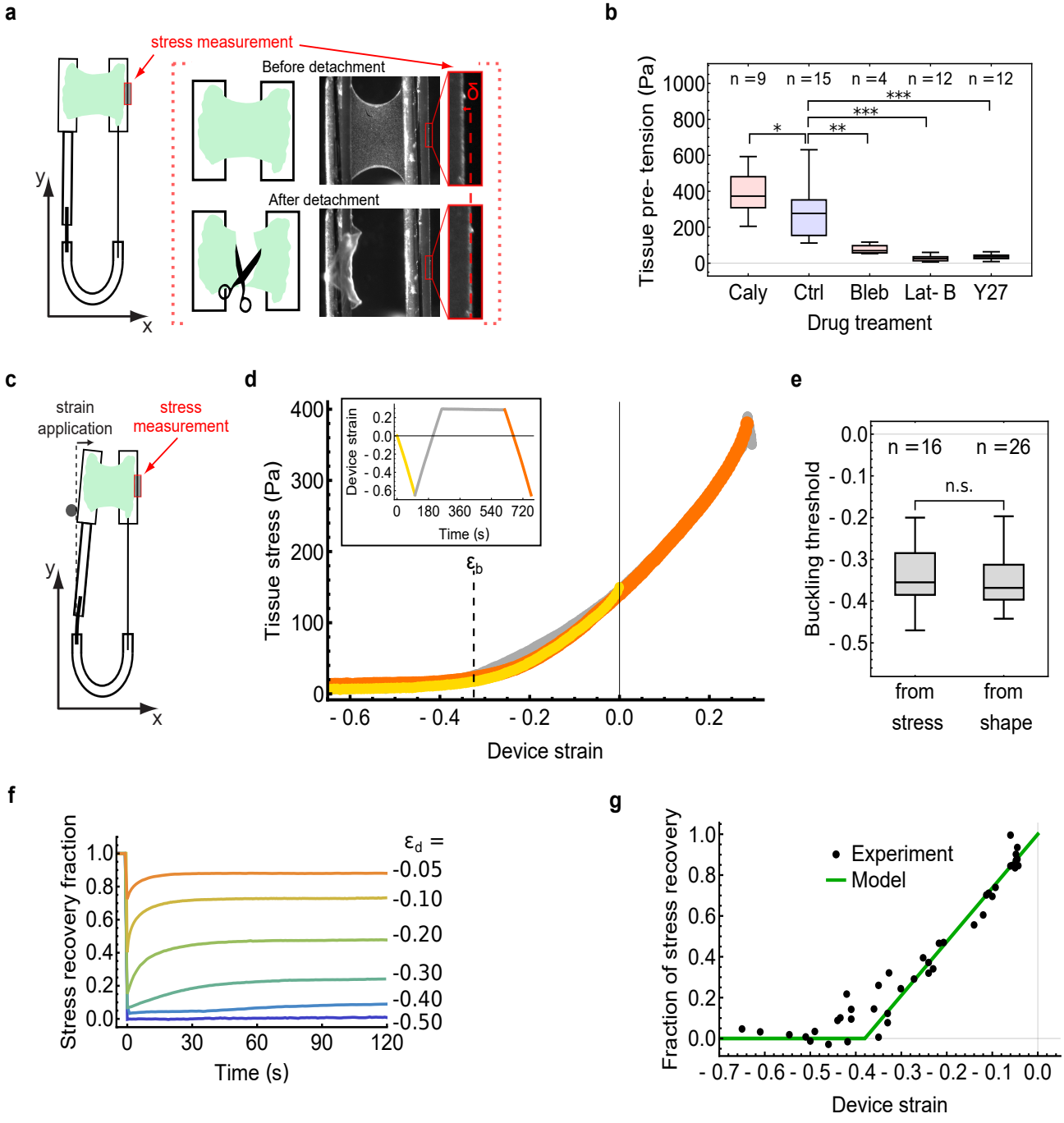
a
stress measurement
Before detachment
After detachment
y
x
b
Tissue pre- tension (Pa)
n =9
n =15
n =4
n =12
n =12
*
**
***
***
Caly
Ctrl
Bleb
Lat- B
Y27
Drug treament
c
strain application
stress measurement
y
x
d
Tissue stress (Pa)
Device strain
Time (s)
εb
e
Buckling threshold
n =16
n =26
n.s.
from stress
from shape
f
Stress recovery fraction
Time (s)
εd =
-0.05
-0.10
-0.20
-0.30
-0.40
-0.50
g
Fraction of stress recovery
Experiment
Model
Device strain

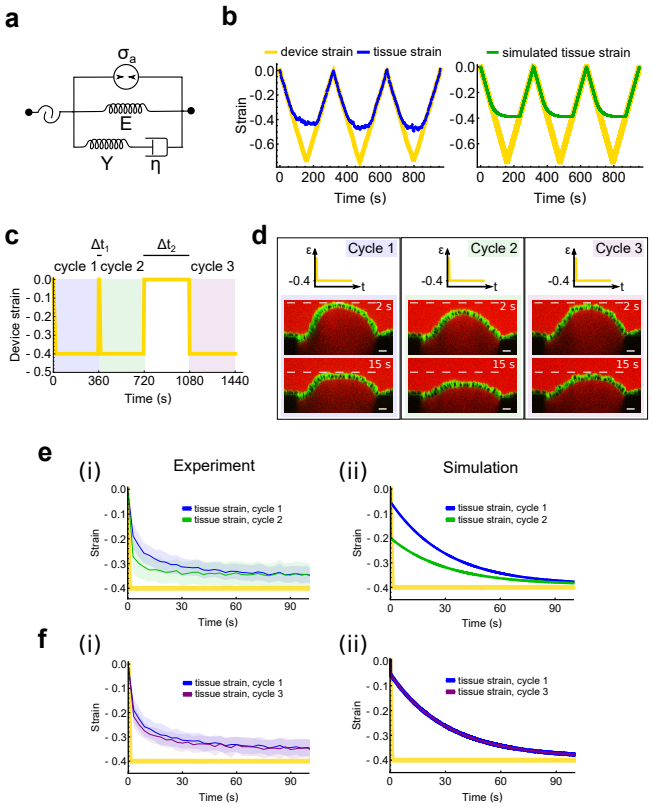
a
σa
E
Y
η
b
device strain
tissue strain
simulated tissue strain
Strain
Time (s)
c
Δt1
Δt2
cycle 1
cycle 2
cycle 3
Device strain
Time (s)
d
Cycle 1
Cycle 2
Cycle 3
ε
t
2 s
15 s
e
(i)
Experiment
(ii)
Simulation
tissue strain, cycle 1
tissue strain, cycle 2
Strain
Time (s)
f
(i)
(ii)
tissue strain, cycle 1
tissue strain, cycle 3
Strain
Time (s)

a

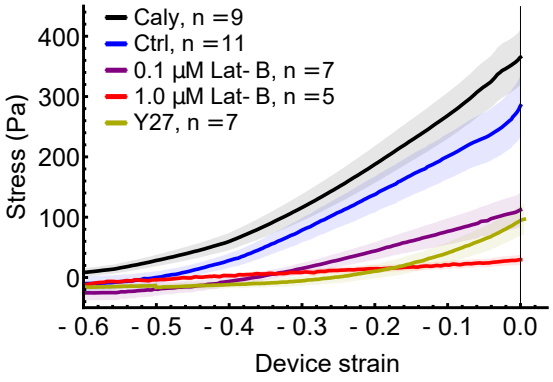
Caly, n =9
Ctrl, n =11
0.1 µM Lat- B, n =7
1.0 µM Lat- B, n =5
Y27, n =7
Stress (Pa)
400
300
200
100
0
- 0.6
- 0.5
- 0.4
- 0.3
- 0.2
- 0.1
0.0
Device strain

b

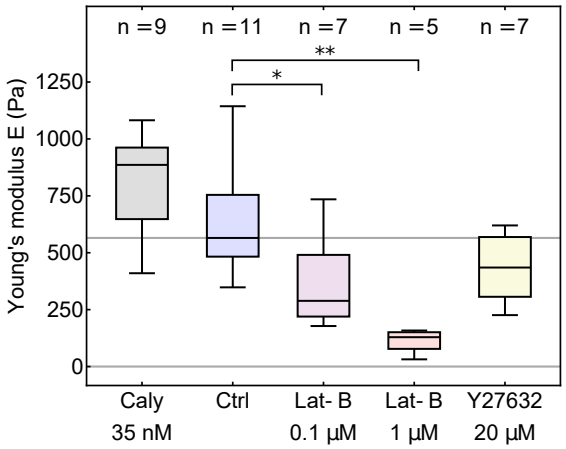
n =9
n =11
n =7
n =5
n =7
**
*
Young's modulus E (Pa)
1250
1000
750
500
250
0
Caly
35 nM
Ctrl
Lat- B
0.1 µM
Lat- B
1 µM
Y27632
20 µM

c

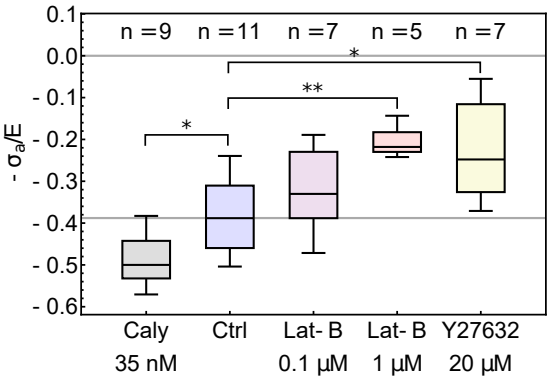
n =9
n =11
n =7
n =5
n =7
*
**
*
- σa/E
0.1
0.0
- 0.1
- 0.2
- 0.3
- 0.4
- 0.5
- 0.6
Caly
35 nM
Ctrl
Lat- B
0.1 µM
Lat- B
1 µM
Y27632
20 µM

d

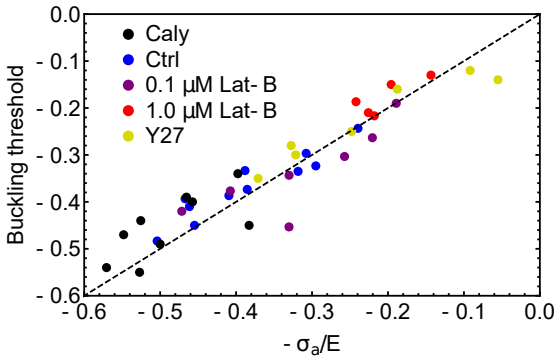
Caly
Ctrl
0.1 µM Lat- B
1.0 µM Lat- B
Y27
Buckling threshold
0.0
- 0.1
- 0.2
- 0.3
- 0.4
- 0.5
- 0.6
- 0.6
- 0.5
- 0.4
- 0.3
- 0.2
- 0.1
0.0
- σa/E

Actomyosin controls planarity and folding of epithelia in response to compression

Tom P. J. Wyatt[†1,2], Jonathan Fouchard[†1], Ana Lisica[1], Nargess Khalilgharibi[1,2], Buzz Baum*[3,4], Pierre Recho[5,6], Alexandre J. Kabla*[6], Guillaume T. Charras*[1,4,7]

†co-first authors: these authors contributed equally.

(1) London Centre for Nanotechnology, University College London, Gower Street, London WC1E 6BT, UK

(2) Centre for Computation, Mathematics and Physics in the Life Sciences and Experimental Biology (CoMPLEX), University College London, Gower Street, London WC1E 6BT, UK

(3) MRC Laboratory for Molecular Cell Biology, University College London, Gower Street, London WC1E 6BT, UK

(4) Institute for the Physics of Living Systems, University College London, Gower Street, London WC1E 6BT, UK

(5) LIPhy, CNRS–UMR 5588, Université Grenoble Alpes, F-38000 Grenoble, France

(6) Department of Engineering, Cambridge University, Cambridge CB2 1PZ, UK

(7) Department of Cell and Developmental Biology, University College London, Gower Street, London WC1E 6BT, UK

*Corresponding authors: Buzz Baum (b.baum@ucl.ac.uk), Alexandre Kabla (ajk61@cam.ac.uk) and Guillaume Charras (g.charras@ucl.ac.uk)

SUPPLEMENTARY VIDEO LEGENDS

Supplementary Video 1| Epithelial response to fast -35% strain application. Buckling and flattening of an MDCK epithelial monolayer in response to a -35% strain applied at high strain rate (500 %.s^{-1}). Cell membranes are marked with CellMask (green), the medium is marked with dextran Alexa-647 (red) to allow for visualisation of the coverslips by dye exclusion. The video is briefly paused on the frame immediately after the application of strain to show the initial shape of the buckled tissue. Scale bar, 20 μm. Time is in mm:ss.

Supplementary Video 2| Epithelial response to fast -50% strain application. Buckling and partial flattening of an MDCK epithelial monolayer in response to a strain of -50% applied at high strain rate (500 %.s^{-1}). Cell membranes are marked with CellMask (green), the medium is marked with dextran Alexa-647 (red) to allow for visualisation of the coverslips by dye exclusion. Scale bar, 20 μm. Time is in mm:ss.

Supplementary Video 3| Epithelial response to slow -80% strain application. Length adaptation and buckling of an MDCK epithelial monolayer in response to compressive strain applied at low strain rate (maximum strain: -80%). Cell membranes are marked with CellMask (green), the medium is marked with dextran Alexa-647 (red) to allow for visualisation of the coverslips by dye exclusion. Scale bar, 20 μm. Time is in mm:ss.

Supplementary Video 4| HaCaT response to fast -35% strain application. Buckling and flattening of a HaCaT epithelial tissue in response to a -35% strain at high strain rate (500 %.s^{-1}). Cell membranes are marked with CellMask (green), the medium is marked with dextran Alexa-647 (red) to allow for visualisation of the coverslips by dye exclusion. Scale bar, 20 μm. Time is in mm:ss.

Supplementary Video 5| HaCaT response to fast -50% strain application. Buckling and partial flattening of a HaCaT epithelial tissue in response to strain of -50% applied at high strain rate (500 %.s^{-1}). Cell membranes are marked with CellMask (green), the medium is marked with dextran Alexa-647 (red) to allow for visualisation of the coverslips by dye exclusion. Scale bar, 20 μm. Time is in mm:ss.

Supplementary Video 6| HaCaT response to slow -80% strain application. Length adaptation and buckling of a HaCaT epithelial tissue in response to compressive strain

applied at low strain rate (maximum strain: -80%). Cell membranes are marked with CellMask (green), the medium is marked with dextran Alexa-647 (red) to allow for visualisation of the coverslips by dye exclusion. Scale bar, 20 μm. Time is in mm:ss.

Supplementary Video 7| Epithelial flattening requires actomyosin activity. Buckling and partial flattening of an MDCK epithelial monolayer treated with 20 μM blebbistatin in response to application of -40% strain applied at high strain rate. Cell membranes are marked with CellMask (green), the medium is marked with dextran Alexa-647 (red) to allow for visualisation of the coverslips by dye exclusion. Scale bar, 20 μm. Time is in mm:ss.

Supplementary Video 8| Dependence of flattening time on strain history. MDCK monolayers were subjected to the sequence of deformation shown in Fig. 4c. After an initial 6 minute period of compressive strain, the tissue is returned to its initial length for $\Delta t_1 = 3$ seconds and shortened again. Left: Tissue flattening in response to the initial cycle of compressive strain. Right: Faster tissue flattening in response to the second cycle of compressive strain. The video is paused briefly at 2 seconds and 15 seconds to allow comparison of the extent of flattening (see white dashed lines). Cell membranes are marked with CellMask (green), the medium is marked with dextran Alexa-647 (red) to allow for visualisation of the coverslips by dye exclusion. Scale bar, 20 μm. Time is in mm:ss.

Supplementary Video 9| Reversibility of the change in flattening time. MDCK monolayers were subjected to the sequence of deformation shown in Fig. 4c. Before a third cycle of compressive strain, the tissue is returned to its initial length for $\Delta t_2 = 6$ minutes before the application of the third compression. Left: Tissue flattening in response to the initial cycle of compressive strain. Right: Tissue flattening in response to the third cycle of compressive strain. The flattening time is no longer distinguishable from the flattening time during the first cycle. The video is paused briefly at 2 seconds and 15 seconds to allow comparison of the extent of flattening (see white dashed lines). Cell membranes are marked with CellMask (green), the medium is marked with dextran Alexa-647 (red) to allow for visualisation of the coverslips by dye exclusion. Scale bar, 20 μm. Time is in mm:ss.

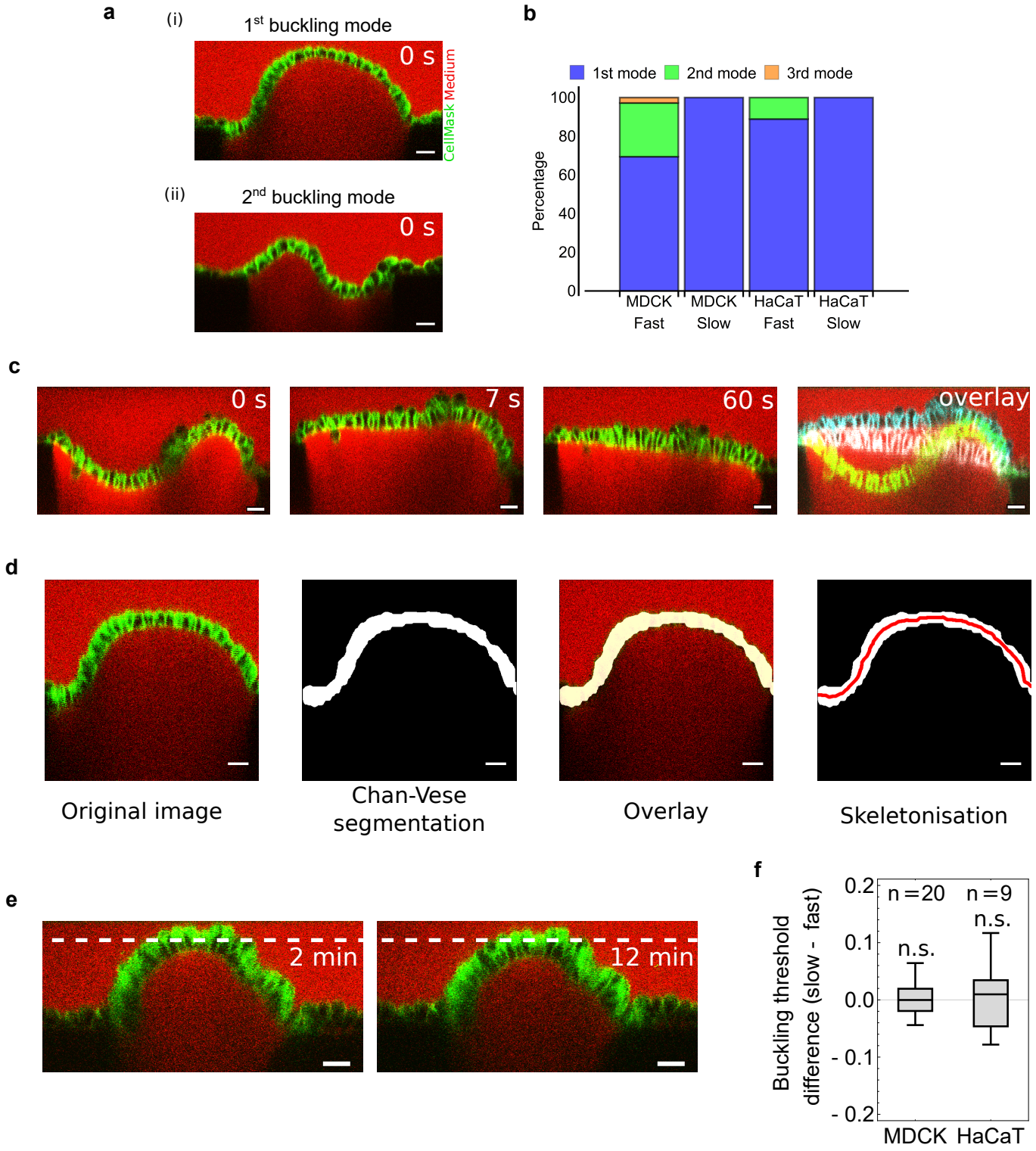

Supplementary Figure 1| Epithelial buckling in response to compression. **a**, Profile view of the two most common tissue shapes observed immediately after application of compressive strain at high strain rate. Cell membranes are marked with CellMask (green), the medium is visualised by addition of dextran Alexa-647 (red). *i*: Most frequently, a single arched shape was produced. *ii*: More complex shapes, reminiscent of the second mode of buckling, were produced in 32% of the cases. Scale bars, 20 μm. **b**, Chart showing the percentage of epithelia which formed buckles resembling different modes during fast (500 $\%.s^{-1}$) or slow (0.5 $\%.s^{-1}$) application of strain. **c**, Time series of profiles of an MDCK epithelium which formed a wave-like shape upon application of -35% strain, which then transitioned to a single arched shape. Right: an overlay of time points 0 s (green), 7 s (cyan) and 60 s (white). Scale bars, 20 μm. **d**, Automated video analysis pipeline for extraction of tissue contour length. The profile image is segmented using the Chan-Vese algorithm. The segmentation is then skeletonised to extract the contour length (right-most image, red line) and tissue strain (see Methods). Scale bars, 20 μm. **e**, Stable fold induced in an MDCK monolayer by application of a device strain larger than the buckling threshold. Folds are stable for more than 10 minutes. The white dashed line demarks the same height in both images. Time after compressive strain application is indicated in the top right corner. Scale bars, 20 μm. **f**, The difference between the buckling threshold measured during a slow ramp of compressive strain and the buckling threshold measured following a step of fast compressive strain applied on the same sample, in a randomised order, for both MDCK and HaCaT epithelia. The number of tissues examined is indicated above the boxplot. (n.s. = not significant).

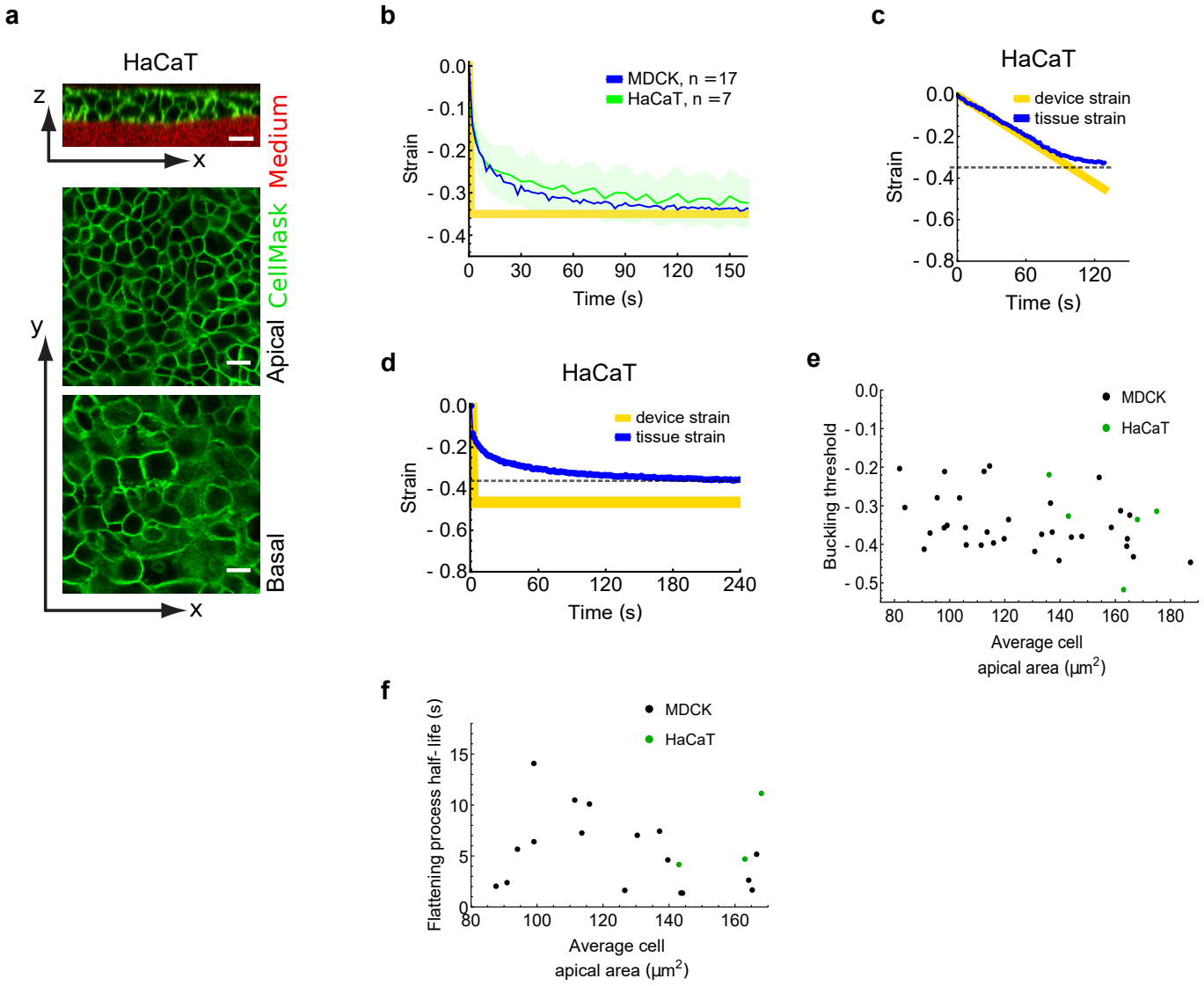

Supplementary Figure 2| Flattening of buckled epithelia in response to compression. **a**, Organisation of a suspended HaCaT tissue. Top: Profile view of the tissue showing multi-layering. Middle: single x-y confocal section of the apical surface of the tissue. Bottom: single x-y confocal section of the basal surface of the tissue. Cell membranes are marked with CellMask (green), the medium is visualised by addition of dextran Alexa-647 (red). Scale bars, 20 μm. **b**, Temporal evolution of tissue strain in MDCK epithelial monolayers (blue, mean ± SD) and HaCaT epithelial tissues (green, mean ± SD) following application of 35% compressive strain at a strain rate of 500 %.s^{-1}. The applied device strain is shown in yellow. Measurements from n = 17 MDCK and n = 7 HaCaT tissues. **c**, Temporal evolution of the tissue strain (blue) during a ramp of device strain (yellow) applied at low strain rate (0.5 %.s $^{-1}$). The dashed line marks the buckling threshold ε_b. **d**, Temporal evolution of the tissue engineering strain resulting from -50% device strain (yellow) applied at a strain rate of 500 %.s^{-1} to a suspended HaCaT epithelium. The dashed line marks the buckling threshold ε_b. **e**, Scatter plot of the buckling threshold of MDCK (black) and HaCaT (green) epithelia plotted against the average cell apical area of the tissue. **f**, Scatter plot of the half-life of flattening in MDCK (black) and HaCaT (green) epithelia plotted against the average cell apical area of the tissue.

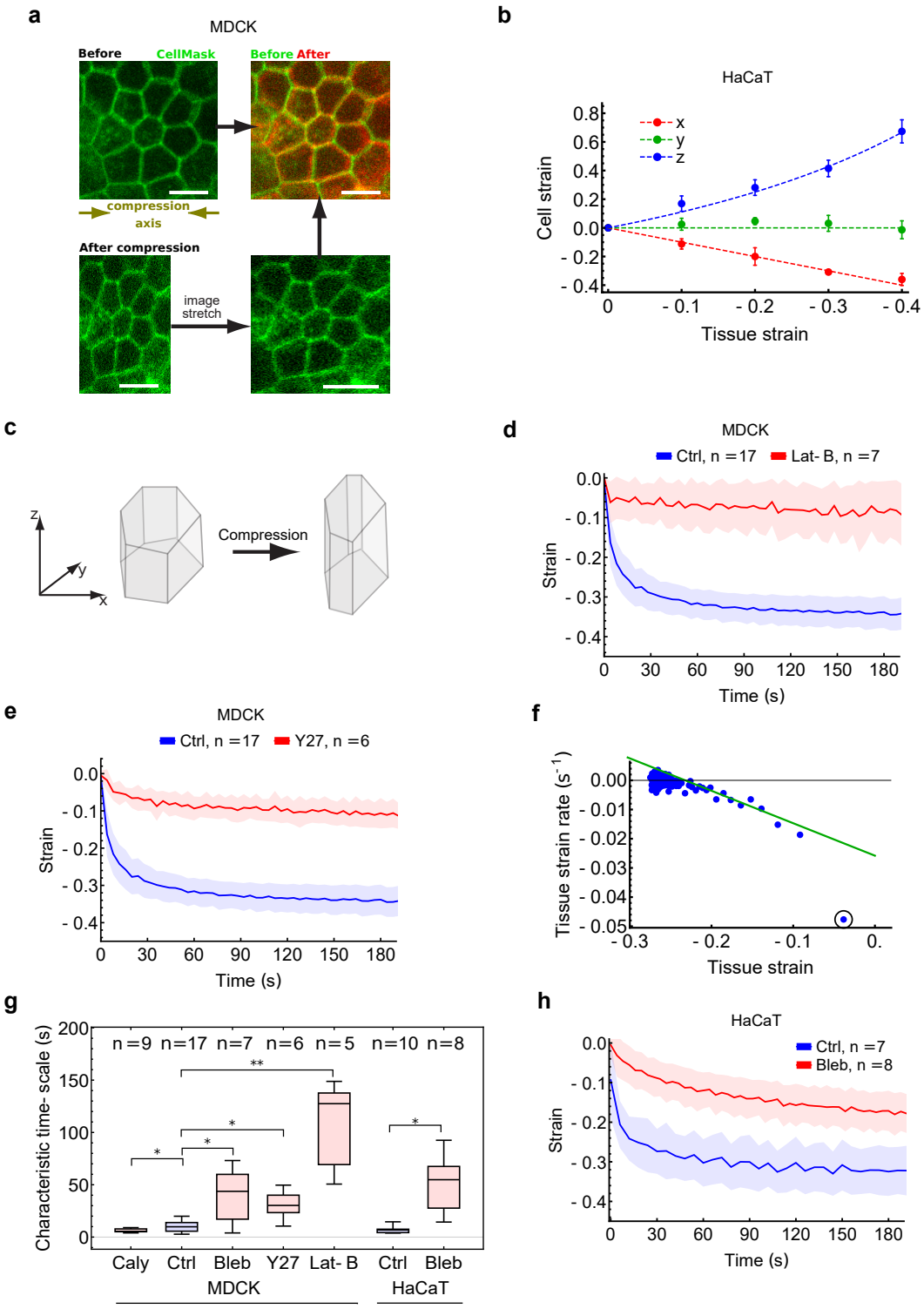

Supplementary Figure 3| Tissue flattening requires cell shape change and actomyosin activity. **a**, Tissue deformation after application of compressive strain is accounted for by isometric cellular deformations. Corresponding regions of cell-cell junctions are imaged before and after application of 30% compressive strain (left column). The image of the compressed tissue is stretched numerically by 30% (bottom right). This image and the image of the tissue before compression are overlaid (top right). Scale bars, 10 μm. **b**, Cellular strain as a function of tissue strain as in Fig. 2b but for HaCaT epithelia. **c**, Diagram depicting the average cell shape change after application of 30% compressive strain. **d**,**e**, Evolution of tissue strain (mean ± SD) following compressive strain applied at high strain rate (500 %.s^{-1}) for control (blue) and treated (red) MDCK tissues. Tissues were treated with 3 μM latrunculin-B (**d**) or 20 μM Y-27632 (**e**). **f**, Extraction of characteristic time-scale of flattening. Tissue strain rate is plotted against tissue strain following fast compression. Tissue strain rate is computed through a linear fit of 3 consecutive time-points of tissue strain. The first points (black circle) do not follow the linear regime and were excluded from the fitting (green line). The characteristic time-scale of the flattening was defined as the negative reciprocal of the linear fit. **g**, Characteristic time-scale of tissue flattening for MDCK and HaCaT tissues. Tissues were treated with drugs altering actomyosin contractility. Caly = calyculin A (35 nM); Bleb = blebbistatin (20 μM for MDCK, 75 μM for HaCaT); Y27 = Y-27632 (10 μM); Lat-B = latrunculin-B (3 μM). Characteristic time-scales were extracted as in (**f**). **h**, Temporal evolution of tissue strain (mean ± SD) following compressive strain applied at high strain rate (500 %.s^{-1}) for control (blue) and treated (red) HaCaT tissues. Tissues were treated with 75 μM blebbistatin.

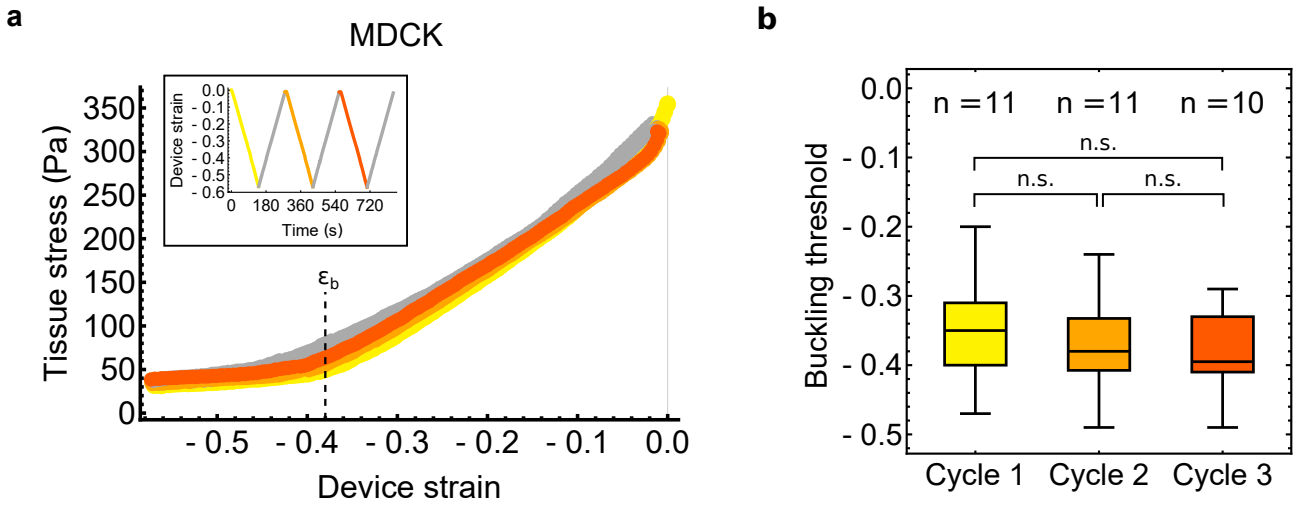

Supplementary Figure 4| Response to compression is consistent over multiple cycles. **a**, Tissue stress as a function of the applied device strain during deformation at low strain rate (0.5 %.s^{-1}) for MDCK epithelia. Inset: Time course of the strain applied with the device. Three cycles of compressive strain were applied. Unloading is indicated in grey. The stress follows the same trend over 3 cycles of compressive strain shown in yellow (1st cycle), orange (2nd cycle) and dark orange (3rd cycle). The dashed line marks the buckling threshold ε_b. **b**, Comparison of the buckling threshold measured from the transition identified in stress-strain curves during each of the three cycles of applied compressive strain. There was no significant difference between the three cycles ($p > 0.2$). The number of tissues examined in each condition is indicated above each box. (n.s. = not significant).

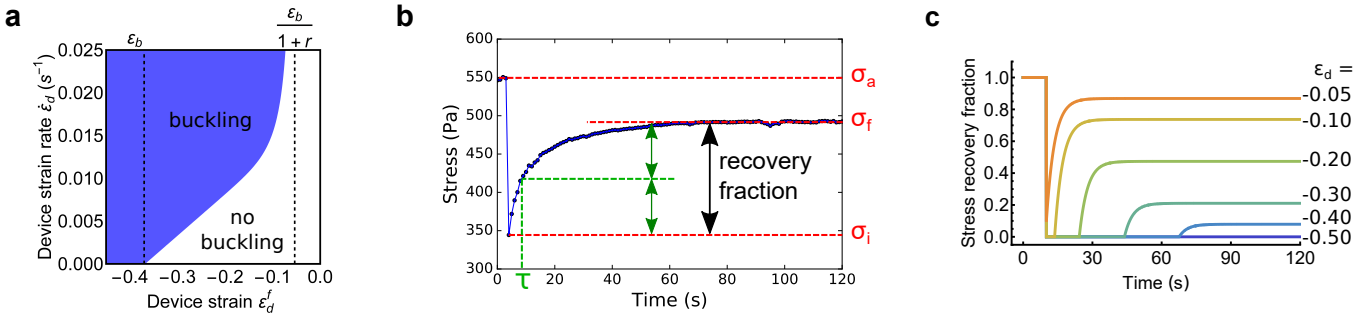

Supplementary Figure 5| Tissue stress recovery after fast compression. **a**, Phase diagram indicating region of the phase space where buckling occurs as a function of the device strain and the device strain rate predicted by the rheological model in Fig. 4a (see Appendix 2 for details). The dashed lines delineate the buckling threshold ε_b (left) and the predicted smallest device strain which can induce a transient buckle (right). r is the ratio between the stiffnesses of the two springs in the model, Y / E. **b**, Representative temporal evolution of stress in response to low amplitude compressive strain applied at high strain rate. Tissue stress values (red) and the recovery time-scale (green) were extracted from the plot as shown and used to calculate the model parameters, as described in Appendix 3. **c**, Simulated tissue response to compressive strain of different magnitudes applied at high strain rate. The magnitude of device strain ε_d is shown on the right. Note the presence of a lag phase at zero stress corresponding to the duration over which the tissue is buckled. This lag phase is more pronounced here in simulations than in experiments.

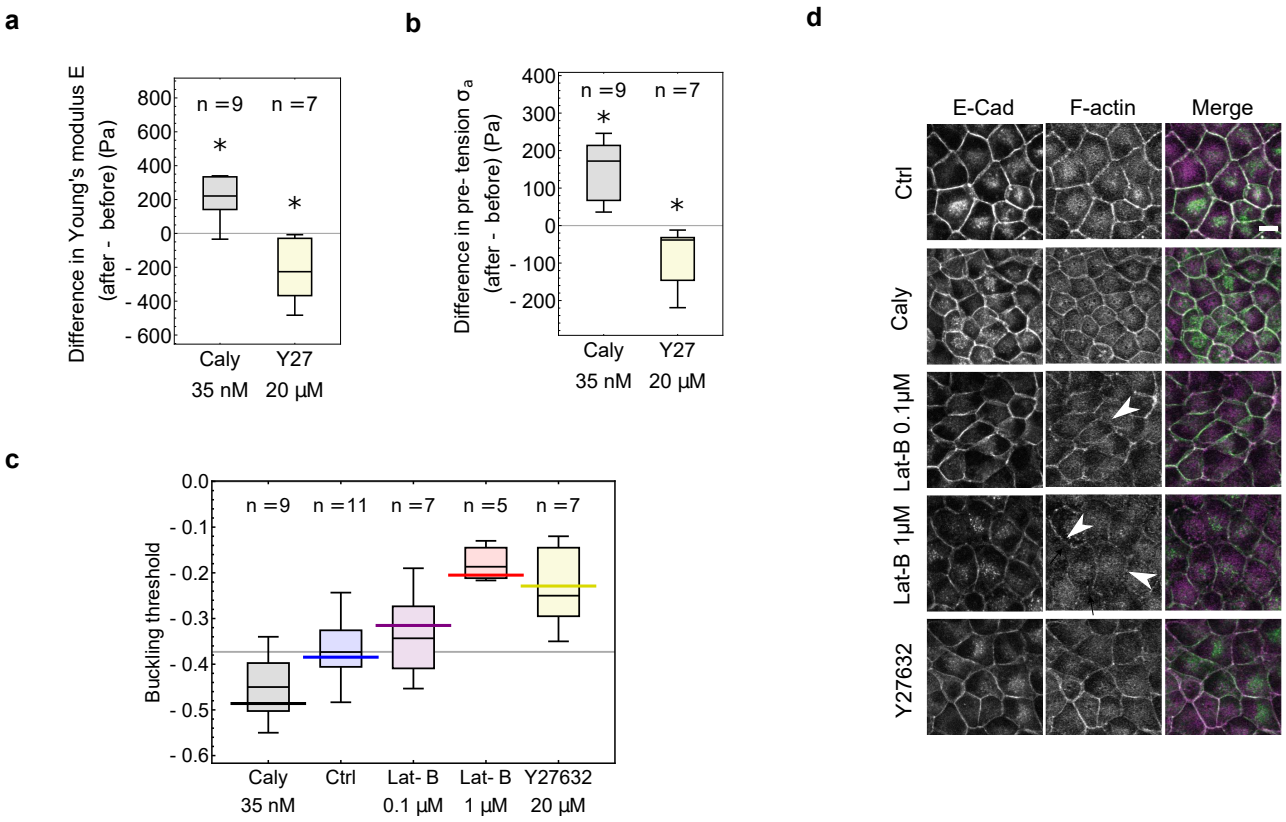

Supplementary Figure 6| Buckling threshold is predicted by pre-tension and stiffness but not junction architecture. a, Difference in Young's modulus E measured on the same MDCK monolayers before and after pharmacological treatments. The treatments were calyculin A (35 nM) and Y-27632 (20 µM). Paired tests mentioned in the main text were derived from this difference. * denotes significant difference from 0 of p = 0.01 (Calyculin) and p = 0.02 (Y-27632). **b**, Difference in tissue pre-tension measured on the same MDCK monolayers before and after pharmacological treatments. * denotes significant difference from 0 of p = 0.01 (Calyculin) and p = 0.02 (Y-27632). **c**, Buckling threshold measured during compressive strain applied at low strain rate (0.1 %.s^{-1}) for control tissues, tissues treated with latrunculin-B (0.1 µM, 1 µM), Y-27632 (20 µM) and calyculin A (35 nM), corresponding to the same samples as in Fig. 5a. The solid coloured bars correspond to the buckling threshold predicted from $-\sigma_a / E$ according to the rheological model shown in Fig. 4a. The number of tissues examined for each treatment is indicated above each box. **d**, Effect of treatments targeting actomyosin on intercellular junction organisation. MDCK ECadherin-GFP (green) cells were stained with phalloidin-Alexa647 to visualise F-actin (magenta). White arrowheads show regions where the junctional F-actin network is disrupted in response to treatment. Scale bar, 10 µm.

SUPPLEMENTARY NOTES

Appendix 1. Interpretation of the observed modes of buckling of epithelia

The quantification of the frequency of occurrence of the different modes of buckling after rapid and slow compression in MDCK and HaCaT tissues revealed that the higher modes were less represented than the first mode when strain was applied at high strain rate (Supplementary Fig. 1a,b). Higher modes were never observed when strain was applied at a low strain rate (Supplementary Fig. 1b). Therefore, the different buckling behaviours depend on the rate of compression. We also observed that the second mode of buckling is always transient, rapidly degenerating into the first mode of buckling during the first few seconds of flattening (Supplementary Fig. 1c). As a result, in experiments at low strain rate, any higher mode buckles would decay into the first mode before they could be observed.

These observations can be explained within the framework of the classical buckling theory where the first mode of buckling is the unique minimum of the system's mechanical free energy. All the other modes are in fact saddle points of that energy and are therefore unstable. As a result, they cannot be steady states. They may still be transiently observed because of small heterogeneities in the material properties (in our case some intrinsic disorder in the cell cytoskeleton or adhesive properties) or boundary conditions (in particular a potential mismatch in the coverslips' vertical alignment) that favor their appearance. In agreement with this, we observed experimentally that the second mode always degenerates to the first mode of buckling in steady state. The duration of such a transition depends on the characteristic timescale of stress relaxation in the tissue and is therefore expected to increase with an increasing tissue viscosity.

Appendix 2. A 0-D model for simulating the mechanical response of an epithelial tissue to compressive strain

Here, we derive a zero-dimensional model for the evolution of the contour length l of the cross-section of an epithelium, which reproduces the experimentally observed dynamics.

<u>A – Description of the model</u>

Based on experimental observations, we assume that the behaviour of the epithelium can be described by a simple rheological model consisting of three branches in parallel (Fig. 4a). The first branch consists of an active stress contribution $\sigma_a > 0$ which models cellular contractility observed in experiments (Fig. 3b) and brings the material to a tensile state at zero strain. The second branch behaves as a solid with an elastic modulus E, denoting the observed behaviour at long time-scales (Fig. 3d). The third branch behaves as a viscous liquid with an elastic modulus Y and relaxation time τ. The product $Y\tau$ corresponds to a bulk viscosity η. (For simplicity, we chose to simplify the dynamics of the tissue by modelling its relaxation with a single characteristic time τ, as our aim is to capture the effects of the buckling non-linearity and tissue pre-tension on the epithelium dynamics.)

Finally, in line with experimental measurements, we hypothesize that the tissue is unable to sustain any compressive force and buckles when the tissue stress σ reaches zero. This is also consistent with the classical buckling theory. Indeed, in the canonical buckling problem of a clamped elastic sheet of length L and thickness h, the critical Euler stress at which buckling occurs (i.e. at which the flat configuration is no longer stable and the first mode of buckling appears) is given by $P_c = E\frac{4\pi^2 h^2}{3L^2}$ where E is the Young's modulus of the sheet. This result holds if the sheet is sufficiently slender, signifying that $h/L \ll 1$ which corresponds well to our system for which $h/L \approx 10^{-2}$. We can therefore estimate that $P_c \approx 7$ Pa in the case of MDCK monolayers assuming that E = 640 Pa, L = 350 µm, h = 10 µm. Thus, the critical load is much smaller than the typical stresses stemming from compression and contractility of the layer (which are on the order of 10^2-10^3 Pa). Therefore, as a first approximation, we take $P_c \approx 0$ (i.e. buckling occurs as soon as the stress becomes compressive). Note that this assumption leads to different dynamic behaviours depending on whether stresses are tensile or compressive (see cases B1 and B2 below).

<u>B – Constitutive behaviour</u>

We have shown that epithelial tissues can buckle and adopt a contour length that is larger than the device plate-to-plate distance. Thus, we define two different strains in our experiments, one relating to the strain of the epithelial tissue and the other relating to the strain applied with the device:

Tissue strain: $\varepsilon = \frac{l-l_0}{l_0}$ where l is the contour length of the tissue.

Device strain: $\varepsilon_d = \frac{d-l_0}{l_0}$ where d is the plate-to-plate distance.

These two strains are defined with respect to a contour length l_0 which is associated to the initial tissue length before the application of any compression and is equal to the initial plate-to-plate distance. Such a choice implies that, as verified experimentally (Fig. 3b), the initial stress on the coverslips is mainly of active origin.

The response of the material to imposed stress or strain is governed by the following equations:

B1 **–** Under tensile stress:

Stress $\sigma > 0$: $\frac{\sigma}{E} = \varepsilon - \varepsilon_b + r\varepsilon_1$ with $r = \frac{Y}{E}$, $\varepsilon_b = \frac{-\sigma_a}{E} < 0$ and ε_1 the internal strain in the spring E which satisfies the equation:

$$\dot{\varepsilon_1} + \frac{\varepsilon_1}{\tau} = \dot{\varepsilon} \qquad (1)$$

- *Strain*: $\varepsilon = \varepsilon_d$

B2 **–** Under compressive stress:

Stress: $\sigma = 0$, this is an assumption of the model based on experimental measurements.

- *Strain*: $\varepsilon = \varepsilon_b - r\varepsilon_1$, where ε_1 satisfies the same equation as in B1. Note that in this case $l > d$ i.e. $\varepsilon > \varepsilon_d$.

C – Steady state behaviour

To begin with, we compute the stress versus device strain, and the tissue strain versus device strain relation $\sigma(\varepsilon_d)$ and $\varepsilon(\varepsilon_d)$ in steady state. This behaviour corresponds to the compressions performed at 0.5 %.s^{-1} and below (see Fig. 1b (iii and vi), Fig. 1f, Fig. 3d, Fig. 4b and Fig. 5a). When the driving parameter ε_d changes at a low rate, the viscous branch does not contribute, and we obtain the following relation: $\sigma/E = \varepsilon_d - \varepsilon_b$, if $\sigma > 0$**.**

This relation is valid until the tissue reaches its buckling threshold for $\varepsilon_d = \varepsilon_b$. At this point, the stress in the tissue vanishes. For $\varepsilon_d < \varepsilon_b$, the stress remains at zero (Fig. 3d, 5a). Similarly, for the tissue strain, $\varepsilon = \varepsilon_d$ as long as $\varepsilon_d > \varepsilon_b$and plateaus at ε_b for $\varepsilon_d \leq \varepsilon_b$.

D – Response of the epithelium to a step of compressive strain

Next, starting from a tissue at its original length, we abruptly shorten it and determine the transitory regime towards establishment of the steady-state stress computed above. The step shortening occurs at t = 0 and changes the device strain from $\varepsilon_d = 0$ to $\varepsilon_d = \varepsilon_d^f$. The initial stress state is σ_a. We then distinguish three cases depending on the magnitude of compressive strain. Supplementary Fig. 5c shows the evolution in a range of magnitudes of device strain.

D1 **–** Case 1 (low device strain): $\varepsilon_d^f > \frac{\varepsilon_b}{1+r}$

In this case, stress in the tissue is always positive and the tissue never buckles. The stress relaxes exponentially. We have:

- *Stress:* $\frac{\sigma(t)}{E} = \varepsilon_d^f - \varepsilon_b + r\varepsilon_d^f e^{-t/\tau}$
- *Strain:* $\varepsilon(t) = \varepsilon_d^f$

D2 **–** Case 2 (intermediate device strain): $\varepsilon_b < \varepsilon_d^f < \frac{\varepsilon_b}{1+r}$

This case corresponds to the experiments shown in Fig. 1b (i and iv) and Fig. 1c. Here, the tissue reaches zero stress and buckles immediately after the step of device strain. After the flattening of the tissue (Phase 1), the tissue returns to a tensional stress state (Phase 2). We thus split the dynamics into two phases:

- *Phase 1 - Stress:* $\sigma = 0$

  - Strain: $\varepsilon(t) = \varepsilon_b\left(1 - \frac{r}{1+r}e^{\frac{-t}{\tau(1+r)}}\right)$
- *Transition time:* Phase 1 comes to an end when ε reaches ε_d^f at time: $T = (1+r)\tau log\left(\frac{\varepsilon_b r}{\left(\varepsilon_b - \varepsilon_d^f\right)(1+r)}\right)$
- *Phase 2 - Stress:* $\frac{\sigma(t)}{E} = \left(\varepsilon_d^f - \varepsilon_b\right)\left(1 - e^{-(t-T)/\tau}\right)$

  - Strain: $\varepsilon(t) = \varepsilon_d^f$

D3 – Case 3 (large device strain): $\varepsilon_d^f < \varepsilon_b$

This case corresponds to the experiments shown in Fig. 1b (ii and v) and Fig. 1d. In this case, the tissue buckles immediately after strain application but cannot flatten sufficiently to restore positive stress. Thus we have:

- *Stress:* $\sigma(t) = 0$
- *Strain:* $\varepsilon(t) = \varepsilon_b\left(1 - \frac{r}{1+r}e^{\frac{-t}{\tau(1+r)}}\right)$

Note that ε converges to the value ε_b for large times indicating that the tissue remains longer than the coverslip-to-coverslip distance, forming a stable fold.

E – Response to cycles of compressive strain

To investigate the duration over which an epithelial tissue can 'remember' its previous mechanical state, we apply a sequence of cycles of compressive strain. From the initial state, the device strain is initially shortened to ε_d^f. This is followed, after a time $T_1 > T$, by a lengthening of $-\varepsilon_d^f$ back to the initial length which is maintained for a duration Δ_1. This is then followed by second cycle of shortening back to ε_d^f. The magnitude of the step of shortening ε_d^f is chosen to be in D-Case 2 so that the contour length shows a relaxation dynamic which is not instantaneous while still reaching a final shape of the tissue that is flat.

In general, because the visco-elastic branch could not fully relax during the period of lengthening, immediately after the second shortening (occurring at $t = T_1 + \Delta_1$), the value of the tissue strain is:

$$\varepsilon = \frac{\varepsilon_b + r\alpha\varepsilon_d^f}{1+r} \tag{2}$$

where $\alpha = e^{-\Delta_1/\tau}$.

This leads to a second recovery with different dynamics that is of the form:

$$\varepsilon(t) = \varepsilon_b + \frac{r\left(\alpha\varepsilon_d^f - \varepsilon_b\right)}{1+r} e^{\frac{-t-(T_1+\Delta_1)}{\tau(1+r)}} \tag{3}$$

until ε reaches ε_d^f after a duration of:

$$T_\alpha = (1+r)\tau log\left(\frac{r\left(\varepsilon_b - \alpha\varepsilon_d^f\right)}{\left(\varepsilon_b - \varepsilon_d^f\right)(1+r)}\right) \tag{4}$$

F – Evolution of the transient buckling point with device strain and strain rate

We now consider the effect of the device strain rate on the buckling properties of the epithelium. This is in order to establish the phase diagram of Supplementary Fig. 5a, defining the planar or buckled state of the tissue with respect to the device strain and strain rate imposed on tissue boundaries.

For this, instead of assuming instantaneous shortening, we impose a ramp of deformation at constant strain rate:

$$\varepsilon_d(t) = \begin{cases} -\dot{\varepsilon}_d t & if \quad t \leq -\varepsilon_d^f/\dot{\varepsilon}_d \\ \varepsilon_d^f & if \quad t \geq -\varepsilon_d^f/\dot{\varepsilon}_d \end{cases} \tag{5}$$

where $\dot{\varepsilon}_d$ is the (positive) device strain rate. We then ask what are the conditions such that buckling occurs during the shortening phase. Using the expression for $\varepsilon_d(t)$, starting from a tensile state, we compute the time dependent stress:

$$\frac{\sigma(t)}{E} = -\dot{\varepsilon}_d t - \varepsilon_b + \tau r \dot{\varepsilon}_d \left(1 - e^{-t/\tau}\right) \tag{6}$$

This stress monotonically decreases in time and we then ask if there is a value of time $t^a \in [0, -\varepsilon_d^f/\dot{\varepsilon}_d]$ in the interval of shortening such that σ reaches zero**.**

An analytical result can be derived in two limiting cases. When $\tau\dot{\varepsilon}_d \ll 1$ (i.e. device strain rate is very slow), we expect t^a to be much larger than τ. Thus

$$0 = -\dot{\varepsilon} t^a - \varepsilon_b \tag{7}$$

and $t^a \leq -\varepsilon_d^f/\dot{\varepsilon}_d$ leads to the buckling condition $\varepsilon_d^f \leq \varepsilon_b$.
This is indeed the condition we expect during quasi-static shortening.

When, on the contrary, $\tau\dot{\varepsilon}_d \gg 1$,

$$0 = -\acute{\varepsilon} t^a - \varepsilon_b - r\dot{\varepsilon} t^a \tag{8}$$

and the condition $t^a \leq -\varepsilon_d^f/\dot{\varepsilon}$ leads to the buckling condition $\varepsilon_d^f < \frac{\varepsilon_b}{1+r}$ which is the one derived in the previous section when considering a sudden shortening. The general case is shown in Supplementary Fig. 5a.

Appendix 3. Determination of model parameters from experiments

The model contains 4 parameters, which we extract as follows:

- The pre-stress in the tissue σ_a corresponds to the stress as measured before any mechanical perturbation is applied to the tissue, i.e at zero strain (Fig. 3b) and is measured as $\sigma_a = 240 \pm 30$ Pa.

- The elasticity E of the tissue was extracted from the slope of the linear phase in slow compression experiments (Fig. 3d) and found to be $E = 640 \pm 80$ Pa.

The two other parameters were extracted from stress relaxation experiments at low device strains (ε_d ≤ 10%, n = 8, Supplementary Fig. 5b). At these strains, the model predicts that the tissue does not buckle and that the stress relaxation follows a single exponential (see Appendix 2, Part D, Case 1).

- The elastic constant Y in the viscous branch is extracted from the peak value of the stress σ_i immediately after the fast step of device strain:

$$Y = \frac{\sigma_i - \sigma_a}{\varepsilon_d} - E \tag{9}$$

  Here, the elasticity E of each sample is extracted from the steady-state value of the stress σ_f in the plateau region (from 100 to 300s, Supplementary Fig. 5b) and through the relation:

$$E = \frac{\sigma_f - \sigma_a}{\varepsilon_d} \tag{10}$$

  We verified that the value of E obtained through this method is the same on average as the one we could extract from the slope of the first phase in the low strain rate experiments. In this manner we measured $Y = 4770 \pm 760$ Pa.

- The time-scale $\tau = Y\eta$ was extracted from the characteristic time-scale of stress recovery. An exponential fit function could not perfectly capture the fast stress relaxation occurring at very short time-scales. Therefore, we defined τ as the half-life of stress recovery (see Supplementary Fig. 5b) and found it to be $\tau = 4.1 \pm 0.7$ s.

The average values of these parameters were introduced in the equations derived in Appendix 2 to perform the *in silico* experiments shown in Fig. 4 and Supplementary Fig. 5c.

Appendix 4. Buckling properties of epithelial sheets in presence of a thin extra-cellular matrix.

In this article, we study the buckling of epithelia devoid of a substrate. We can thus ask how our results could be affected by the presence of a substrate consisting of extra-cellular

matrix (ECM). As an important initial limitation, we must highlight that the epithelial behaviors will be entirely different in cases where ECM is present as a very thick layer, that is, when the ECM thickness is of the same order of magnitude as the tissue length L. This limit represents the case where the ECM should be treated as a (poro)-elastic foundation which would entirely suppress buckling of the epithelium if the tissue and the ECM are adherent. However, in this extreme case, our work still highlights the fact that a pre-tensional state will allow epithelia to be subjected to compressive strain without entering compressive stress. From our results, it is also possible to estimate the rate at which compression could be applied to such an epithelium before compressive stresses were induced. We speculate that compressive stresses could cause damage to the epithelium at the cellular level or drive detachment of the cell layer from the ECM.

We therefore concentrate on the case of a thin layer of ECM, of thickness e, where $e/L \ll 1$. In this case, the presence of the ECM in parallel to the cells will modify the effective stiffness of the composite and the critical stress at which buckling occurs. In the presence of such a thin foundation, the expression of the critical stress at which buckling occurs now reads: $P_c = E\frac{\pi^2}{3L^2}\left(\frac{h^3}{h+e} + 3h(h+e) + \frac{E_{ecm}}{E}\frac{e^3}{h+e}\right)$[1], where E_{ecm} is the Young modulus of the ECM and *h* the thickness of the epithelium. In the case of Matrigel, $E_{ecm} \approx 450$ Pa which is of the same order of magnitude as our measured E for the epithelia[2]. As a result, for the presence of ECM to strongly impact our assumption that $P_c \approx 0$, we need to have $e \gg h$ such that the last term of P_c becomes dominant and e/L becomes of order one. This places us in the case that we described in the paragraph above. Therefore, for $e/L \ll 1$, any change in the critical buckling stress due to the presence of an ECM can be neglected when applying our results.

A second effect of the presence of a thin layer of ECM is to modify the effective Young's modulus of the cell-ECM composite. This can be taken into account directly in our 0-D model (Fig 4a) by adding a spring in parallel with E which represents the long-term stiffness of the epithelium. The model is then affected only by the fact that E should be replaced by the effective stiffness $E' = \frac{h}{h+e}E + \frac{e}{h+e}E_{ecm}$. All tissue behaviors studied in our work will remain qualitatively the same but the precise values of both the buckling strain $\varepsilon_a = -\sigma_a/E'$ and the relaxation parameter $r = Y/E'$ will change accordingly. Since E_{ecm} is expected to be of the same order of magnitude as E, we only expect to find significant quantitative effects as the ECM thickness approaches a thickness comparable to tissue thickness.

As an example, in the lung, the thickness of the ECM varies from a couple of hundred nanometers for the basement membrane of the alveolae[3] to approximately 5 µm in the case of bronchial epithelium[4], while our tissues are 10-15 µm thick. Therefore, lung tissues represent clear cases in which our results are relevant and could be used to help predict and/or interpret tissue behavior.

SUPPLEMENTARY REFERENCES

1. Huang, H. & Kardomateas, G. A. A. Buckling and Initial Postbuckling Behavior of Sandwich Beams Including Transverse Shear. *AIAA J.* **40,** 2331–2335 (2002).
2. Soofi, S. S., Last, J. A., Liliensiek, S. J., Nealey, P. F. & Murphy, C. J. The elastic modulus of Matrigel as determined by atomic force microscopy. *J. Struct. Biol.* **167,** 216–219 (2009).
3. Weibel, E. R. On the tricks alveolar epithelial cells play to make a good lung. *Am. J. Respir. Crit. Care Med.* **191,** 504–513 (2015).
4. Watanabe, K., Senju, S., Toyoshima, H. & Yoshida, M. Thickness of the basement membrane of bronchial epithelial cells in lung diseases as determined by transbronchial biopsy. *Respir. Med.* **91,** 406–410 (1997).